

MODELING THE METALLICITY DISTRIBUTION OF GLOBULAR CLUSTERS

ALEXANDER L. MURATOV AND OLEG Y. GNEDIN

University of Michigan, Department of Astronomy, Ann Arbor, MI 48109
muratov@umich.edu, ognedin@umich.edu

(Dated: October 22, 2018)

Accepted to ApJ

ABSTRACT

Observed metallicities of globular clusters reflect physical conditions in the interstellar medium of their high-redshift host galaxies. Globular cluster systems in most large galaxies display bimodal color and metallicity distributions, which are often interpreted as indicating two distinct modes of cluster formation. The metal-rich and metal-poor clusters have systematically different locations and kinematics in their host galaxies. However, the red and blue clusters have similar internal properties, such as the masses, sizes, and ages. It is therefore interesting to explore whether both metal-rich and metal-poor clusters could form by a common mechanism and still be consistent with the bimodal distribution. We present such a model, which prescribes the formation of globular clusters semi-analytically using galaxy assembly history from cosmological simulations coupled with observed scaling relations for the amount and metallicity of cold gas available for star formation. We assume that massive star clusters form only during mergers of massive gas-rich galaxies and tune the model parameters to reproduce the observed distribution in the Galaxy. A wide, but not entire, range of model realizations produces metallicity distributions consistent with the data. We find that early mergers of smaller hosts create exclusively blue clusters, whereas subsequent mergers of more massive galaxies create both red and blue clusters. Thus bimodality arises naturally as the result of a small number of late massive merger events. This conclusion is not significantly affected by the large uncertainties in our knowledge of the stellar mass and cold gas mass in high-redshift galaxies. The fraction of galactic stellar mass locked in globular clusters declines from over 10% at $z > 3$ to 0.1% at present.

Subject headings: galaxies: formation — galaxies: star clusters — globular clusters: general

1. INTRODUCTION

A self-consistent description of the formation of globular clusters remains a challenge to theorists. A particularly puzzling observation is the apparent bimodality, or even multimodality, of the color distribution of globular cluster systems in galaxies ranging from dwarf disks to giant ellipticals (reviewed by Brodie & Strader 2006). This color bimodality likely translates into a bimodal distribution of the abundances of heavy elements such as iron. We know this to be the case in the Galaxy as well as in M31, where relatively accurate spectral measurements exist for a large fraction of the clusters. In this paper we will interchangeably refer to metal-poor clusters as blue clusters, and to metal-rich clusters as red clusters.

Bimodality in the globular cluster metallicity distribution of luminous elliptical galaxies was proposed by Zepf & Ashman (1993), following a theoretical model of Ashman & Zepf (1992). The concept of cluster bimodality became universally accepted because the two populations also differ in other observed characteristics. The system of red clusters has a significant rotation velocity similar to the disk stars whereas blue clusters have little rotational support, in the three disk galaxies observed in detail: Milky Way, M31, and M33 (Zinn 1985). In elliptical galaxies, blue clusters have a higher velocity dispersion than red clusters, both due to lack of rotation and more extended spatial distribution. Red clusters are usually more spatially concentrated than blue clusters (Brodie & Strader 2006). All of these differences, however, are in external properties (location and kinematics), which reflect *where* the clusters formed, but not *how*. The internal properties of the red and blue clusters are similar: masses, sizes, and ages, with only slight differences. Even the metallicities themselves differ typically by a factor of 10 between

the two modes, not enough to affect the dynamics of molecular clouds from which these clusters formed. Could it be then that both red and blue clusters form in a similar way on small scales, such as in giant molecular clouds, while the differences in their metallicity and spatial distribution reflect when and where such clouds assemble?

All scenarios proposed in the literature assumed different formation mechanisms for the red and blue clusters, and most scenarios envisioned the stellar population of one mode to be tightly linked to that of the host galaxy (e.g., Forbes et al. 1997; Cote et al. 1998; Strader et al. 2005; Griffen et al. 2010). The other mode is assumed to have formed differently, in some unspecified “primordial” way. This assumption only pushed the problem back in time but it did not solve it. For example, Beasley et al. (2002) used a semi-analytical model of galaxy formation to study bimodality in luminous elliptical galaxies and needed two separate prescriptions for the blue and red clusters. In their model, red clusters formed in gas-rich mergers with a fixed efficiency of 0.007 relative to field stars, while blue clusters formed in quiescent disks with a different efficiency of 0.002. The formation of blue clusters also had to be artificially truncated at $z = 5$. Strader et al. (2005), Rhode et al. (2005), and Griffen et al. (2010) suggested that the blue clusters could instead have formed in very small halos at $z \gtrsim 10$, before cosmic reionization removed cold gas from such halos. This scenario requires high efficiency of cluster formation in the small halos and also places stringent constraints on the age spread of blue clusters to be less than 0.5 Gyr. Unfortunately, even the most recent measurements of relative cluster ages in the Galaxy (De Angeli et al. 2005; Marín-Franch et al. 2009; Dotter et al. 2010) cannot detect age differences smaller than

9%, or about 1 Gyr, and therefore cannot support or falsify the reionization scenario. Dotter et al. (2010) also show that the red clusters have larger dispersion of ages (15%, or about 2 Gyr) and those located outside 15 kpc of the Galactic center tend to show measurably lower ages, by as much as 50% (or 6 Gyr). In addition, Strader et al. (2009) find that the red clusters in M31 have lower mass-to-light ratios than the blue clusters, possibly indicating an age variation.

In this paper we set out to test whether a common mechanism could explain the formation of both modes and produce an entire metallicity distribution consistent with the observations. We begin with a premise of the hierarchical galaxy formation in a Λ CDM universe. Hubble Space Telescope observations have convincingly demonstrated one of the likely formation routes for massive star clusters today – in the mergers of gas-rich galaxies (e.g., Holtzman et al. 1992; O’Connell et al. 1995; Whitmore et al. 1999; Zepf et al. 1999). We adopt this single formation mechanism for our model and assume that clusters form only during massive gas-rich mergers. We follow the merging process of progenitor galaxies in a Galaxy-sized environment using a set of cosmological N -body simulations. We need to specify what type and how many clusters will form in each merger event. For this purpose, we use observed scaling relations to assign each dark matter halo a certain amount of cold gas that will be available for star formation throughout cosmic time and an average metallicity of that gas. In order to keep the model transparent, we choose as simple a parametrization of the cold gas mass as possible. Finally, we make the simplest assumption that the mass of all globular clusters formed in the merger is linearly proportional to the mass of this cold gas.

Although such model appears extremely simplistic, we have some confidence that it may capture main elements of the formation of massive clusters. Kravtsov & Gnedin (2005) used a cosmological hydrodynamic simulation of the Galactic environment at high redshifts $z > 3$ and found dense, massive gas clouds within the protogalactic disks. If the high-density regions of these clouds formed star clusters, the resulting distributions of cluster mass, size, and metallicity are consistent with those of the Galactic metal-poor clusters. In that model the total mass of clusters formed in each disk was roughly proportional to the available gas mass, $M_{GC} \propto M_g$, just as we assume here.

We tune the parameters of our semi-analytical model to reproduce the metallicity distribution of the Galactic globular clusters, as compiled by Harris (1996). This distribution is dominated by the metal-poor clusters but is also significantly bimodal. We attempt to construct a model without explicitly differentiating the two modes and test if bimodality could arise naturally in the hierarchical framework.

We adopt a working definition of red clusters as having $[\text{Fe}/\text{H}] > -1$ and blue clusters as having $[\text{Fe}/\text{H}] < -1$. This definition should also roughly apply to extragalactic globular cluster systems. We use the concordance cosmology with $\Omega_0 = 0.3$, $\Omega_\Lambda = 0.7$, $h = 0.7$.

2. PRESCRIPTION FOR GLOBULAR CLUSTER FORMATION

2.1. Cold Gas Fraction

We follow the merging process of protogalactic dark matter halos using cosmological N -body simulations of three Milky Way-sized systems described in Kravtsov et al. (2004). The simulations were run with the Adaptive Refinement Tree code

(Kravtsov et al. 1997) in a $25 h^{-1}$ Mpc box. Specifically, we use merger trees for three large host halos and their corresponding subhalo populations. The three host halos contain $\sim 10^6$ dark matter particles and have virial masses $\sim 10^{12} M_\odot$ at $z = 0$. Two halos are neighbors, located at 600 kpc from each other. The configuration of this pair resembles that of the Local Group. The third halo is isolated and is located 2 Mpc away from the pair. All three systems experience no major mergers at $z < 1$ and thus could host a disk galaxy like the Milky Way.

In addition to the host halos, the simulation volume contains a large number of dwarf halos that begin as isolated systems and then at some point accrete onto the host halo. Some of these satellites survive as self-gravitating systems until the present, while the rest are completely disrupted by the tidal forces. We allow both the host and the satellite systems to form globular clusters in our model.

We adopt a simple hypothesis, motivated by the hydrodynamic simulation of Kravtsov & Gnedin (2005), that the mass in globular clusters, M_{GC} , that forms in a given protogalactic system is directly proportional to the mass of cold gas in the system, M_g . We define the corresponding mass fraction, f_g , of cold gas that will be available for star cluster formation in a halo of mass M_h as

$$f_g \equiv \frac{M_g}{f_b M_h}, \quad (1)$$

where $f_b \approx 0.17$ is the universal baryon fraction (Komatsu et al. 2010).

The gas fraction cannot exceed the total fraction of baryons accreted onto the halo, which is limited by external photoheating and depends on the cutoff mass $M_c(z)$:

$$f_{in} = \frac{1}{(1 + M_c(z)/M_h)^3}. \quad (2)$$

We use an updated version of the cutoff mass as a function of redshift (originally defined by Gnedin 2000), based on our fitting of the results of recent simulations by Hoefft et al. (2006), Crain et al. (2007), Tassis et al. (2008), and Okamoto et al. (2008):

$$M_c(z) \approx 3.6 \times 10^9 e^{-0.6(1+z)} h^{-1} M_\odot. \quad (3)$$

Given the scatter in simulation results and the numerical limitations of the modeling of gas physics, a reasonable uncertainty in this mass estimate is of the order 50%. However, the resulting cluster mass and metallicity distributions are not very sensitive to the exact form of this equation. Note that Orban et al. (2008) provided an earlier revision of the equation for $M_c(z)$; our current form is more accurate. If $M_c(z)$ falls below the mass of a halo with the virial temperature of 10^4 K, we set $M_c(z)$ equal to that mass:

$$M_{c,\min}(z) = M_4 \equiv 1.5 \times 10^{10} \Delta_{\text{vir}}^{-1/2} \frac{H_0}{H(z)} h^{-1} M_\odot, \quad (4)$$

where $\Delta_{\text{vir}} = 180$ is the virial overdensity and $H(z)$ is the Hubble parameter at redshift z . This criterion ensures that we only select halos able to cool efficiently via atomic hydrogen recombination lines.

Some of the baryons accreted onto a halo may be in a warm or hot phase (at $T > 10^4$ K) unavailable for star formation, thus $f_g < f_{in} < 1$. We assume that only the gas in cold phase ($T \ll 10^4$ K) is likely to be responsible for star cluster formation. The cold gas fraction f_g is calculated by combining sev-

eral observed scaling relations. From the results of McGaugh (2005), the average gas-to-stellar mass ratio in nearby spiral and dwarf galaxies can be fitted as

$$\frac{M_g}{M_*} \approx \left(\frac{M_*}{M_s(z)} \right)^{-0.7}, \quad (5)$$

where M_s is a characteristic scale mass, which we found to be $M_s(z=0) \approx 4 \times 10^9 M_\odot$. This relation saturates at low stellar masses, where f_g cannot exceed f_{in} . At higher redshift the only information on the gas content of galaxies comes from the study by Erb et al. (2006) of Lyman break galaxies at $z=2$. These authors estimated the cold gas mass by inverting the Kennicutt-Schmidt law and using the observed star formation rates. These estimates are fairly uncertain and model-dependent. Within the uncertainties, their results can be fitted by the same formula but with a different scale mass: $M_s(z=2) \approx 2 \times 10^{10} M_\odot$. To extend this relation to all epochs, we employ a relation that interpolates the two values:

$$M_s(z) \approx 10^{9.6+0.35z} M_\odot. \quad (6)$$

An additional scaling relation is needed to complement equation (5) with a prescription for stellar mass as a function of halo mass. We compile it by combining the observed stellar mass–circular velocity correlation with the theoretical circular velocity–halo mass correlation. Woo et al. (2008) found that the stellar mass of the dwarf galaxies in the Local Group correlates with their circular velocities, which are taken as the rotation velocity for the irregular galaxies or the appropriately scaled velocity dispersion for the spheroidal galaxies. In the range $10^7 M_\odot < M_* < 10^{10} M_\odot$, appropriate for the systems that may harbor globular clusters, the correlation is $V_c \propto M_*^{0.27 \pm 0.01}$. This can be inverted as $M_* \approx 1.6 \times 10^9 M_\odot (V_c/100 \text{ km s}^{-1})^{3.7}$.

Cosmological N -body simulations show that dark matter halos, both isolated halos and satellites of larger halos, exhibit a robust correlation between their mass and maximum circular velocity (e.g., Fig. 6 of Kravtsov et al. 2004): $V_{\max} \approx 100 (M_h/1.2 \times 10^{11} M_\odot)^{0.3} \text{ km s}^{-1}$. This maximum circular velocity of dark matter is typically lower than the rotation velocity of galaxies because of the contribution of stars and gas. To connect the two velocities, we apply the correction $V_c = \sqrt{2} V_{\max}$, which reflects the observation that the mass in dark matter is approximately equal to the mass in stars over the portions of galaxies that contain the majority of stars. Then the equations in the last two paragraphs lead to $M_* \approx 5.5 \times 10^{10} (M_h/10^{12} M_\odot)^{1.1} M_\odot$.

We also need to extend this local relation to other redshifts. Conroy & Wechsler (2009) matched the observed number densities of galaxies of given stellar mass with the predicted number densities of halos of given mass from $z=0$ to $z \sim 2$, averaged over the whole observable universe. They find that the stellar fraction f_* peaks at masses $M_h \sim 10^{12} M_\odot$ and declines both at lower and higher halo masses. The range of masses of interest to us is below the peak, where we can approximate f_* dependence on halo mass as a power-law. The results from Fig. 2 of Conroy & Wechsler (2009) are best fit by a steeper relation than we derived for the Local Group and also show significant variation with redshift at lower halo masses $\sim 10^{11} M_\odot$: $M_* \propto M_h^{1.5} (1+z)^{-2}$ (there is much less variation with time around the peak at $10^{12} M_\odot$, implying only a weak evolution in the total stellar density at $z < 1$). We adopt the same redshift dependence to our local relation, while using

the shallower slope derived from Woo et al. (2008) because it deals with a population of halos in the mass range corresponding to the Milky Way progenitors. The stellar mass fraction of isolated halos is thus

$$f_* = \frac{M_*}{f_b M_h} \approx 0.32 \left(\frac{M_h}{10^{12} M_\odot} \right)^{0.1} (1+z)^{-2}. \quad (7)$$

This relation steepens at low masses because of two additional limits on the gas and stellar fractions, which we impose to constrain the range of equations (5–7) to be physical.

First, the sum of the gas and stars (“cold baryons”) cannot exceed the total amount of accreted baryons in a halo:

$$f_* + f_g \leq f_{in}. \quad (8)$$

At each redshift, there is a transition mass $M_{h,\text{cold}}$, below which $f_* + f_g = f_{in}$ and above which $f_* + f_g < f_{in}$. For masses $M < M_{h,\text{cold}}$ (but not too low, see next paragraph), we set $f_{g,\text{revised}} = f_{in} - f_*$, with f_* still given by equation (7). We consider the baryons that are not included in f_g or f_* to be in the warm-hot diffuse phase of the interstellar medium.

Second, the ratio of stars to cold baryons, $\mu_* \equiv f_*/(f_* + f_g)$, is not allowed to increase with decreasing halo mass. For massive halos ($M_h > M_{h,\text{cold}}$) μ_* monotonically decreases with decreasing mass because of the condition (5). At some intermediate masses $M_{h,\mu} < M_h < M_{h,\text{cold}}$, μ_* continues to decrease but the gas fraction is reduced by the condition (8). At $M_h < M_{h,\mu}$, μ_* would reverse this trend and increase with decreasing halo mass because the cold gas is almost completely depleted. Such a reversal is unlikely to happen in real galaxies, which would not be able to convert most of their cold gas into stars. Therefore, for all masses $M_h < M_{h,\mu}$ we fix μ_* to be equal to the minimum value reached at $M_{h,\mu}$. This affects both f_* and f_g .

We expect our stellar mass prescription to apply in the range of halo masses from 10^9 to $10^{12} M_\odot$, at least for the Local Group. However, this relation breaks when a halo becomes a satellite of a larger system. Satellite halos often have dark matter in the outer parts stripped by tidal forces of the host, while the stars remain intact in the inner parts. Unless the satellite is completely disrupted, we keep its stellar mass fixed at the value it had at the time of accretion, even though the halo mass may subsequently decrease.

The simultaneous effects of the above scaling relations are difficult to understand as equations. Figure 1 illustrates graphically the values of the gas and stellar fractions used in our model at various cosmic times. At $z=0$ the gas fraction peaks for halos with $M_h \sim 3 \times 10^{10} M_\odot$. At lower masses it is reduced by the amount of accreted baryons (eq. 8), while at higher masses it is reduced by the gas-to-stars ratio (eq. 5). The stellar fraction follows equation (7) at high masses but drops faster at low masses because of the constraint (8). For a Galaxy-mass halo, $M_h \approx 10^{12} M_\odot$, our model gives $M_* \approx 5.5 \times 10^{10} M_\odot$ and $M_g \approx 9 \times 10^9 M_\odot$. These numbers are consistent with the observed amount of the disk and bulge stars and the atomic and molecular gas in the Galaxy, from Binney & Tremaine (2008).

At earlier epochs at all masses of interest, the gas fraction is higher and the stellar fraction is lower. There is a range of halos with $M_h \gtrsim 10^{10} M_\odot$, which have an almost 100% gas fraction at redshifts $z > 3$. Such halos should be most efficient at forming massive star clusters.

We realize that our adopted relations for the evolution of the stellar and gas mass are not unique, as we are basing each

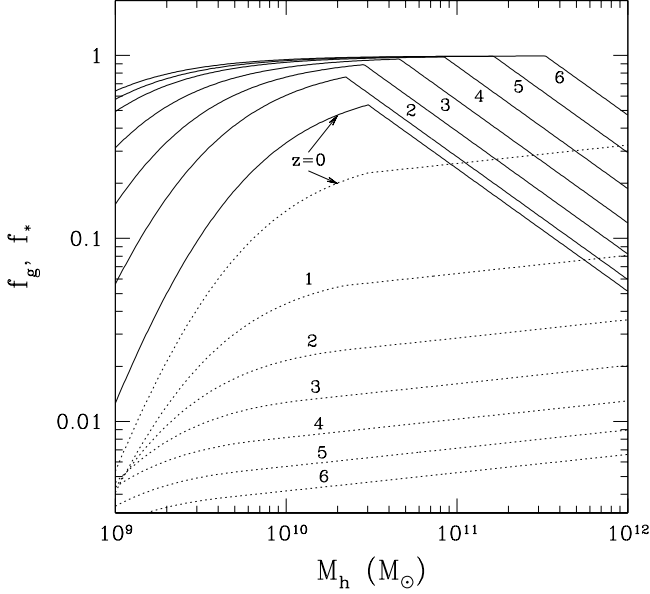


Figure 1. Gas mass fraction (*solid lines*) and stellar mass fraction (*dotted lines*) vs. halo mass in our model at redshifts $z = 0, 1, 2, 3, 4, 5, 6$. Stellar fractions monotonically increase with time while gas fractions decrease with time. The kink in the curves is due to our restriction on the maximum stellar fraction via eq. (8).

fit on two data points. In order to test the sensitivity of our results to these assumptions, we consider alternative functional forms for these fits in Section 4.5. In particular, we give the stellar fraction a steeper dependence on halo mass and weaker dependence on cosmic time:

$$f_{*,\text{alt}} = 0.32 \left(\frac{M_h}{10^{12} M_\odot} \right)^{0.5} (1+z)^{-1}. \quad (9)$$

Such a slower evolution of the stellar mass is consistent with the observational studies of Borch et al. (2006), Bell et al. (2007), and Dahlen et al. (2007). The corresponding gas and stellar fractions are shown in Figure 2. Note that the amount of cold gas available for cluster formation is not strongly affected by this change (compare Figs. 1 and 2).

2.2. Rate of Cluster Formation

Having fixed the parametrization of the available cold gas, we then relate the gas mass of a protogalaxy to the combined mass of all globular clusters it can form within $\sim 10^8$ yr (the timescale of the simulation output). We based it on the rate derived in Kravtsov & Gnedin (2005):

$$M_{GC} = 3 \times 10^6 M_\odot (1+p_2) \frac{M_g/f_b}{10^{11} M_\odot}. \quad (10)$$

An additional factor, $1+p_2$, allows us to boost the rate of cluster formation. Such a boost may be needed because we form new clusters only at arbitrarily chosen epochs corresponding to the simulation outputs. Unresolved mergers between the outputs may require $p_2 > 0$. In our model we find the best fit to the Galactic metallicity distribution for $p_2 \sim 3$ (see Table 1).

Note also that equation (10) imposes the minimum mass of a halo capable of forming a globular cluster. Based on dynamical disruption arguments (Section 3) we track only

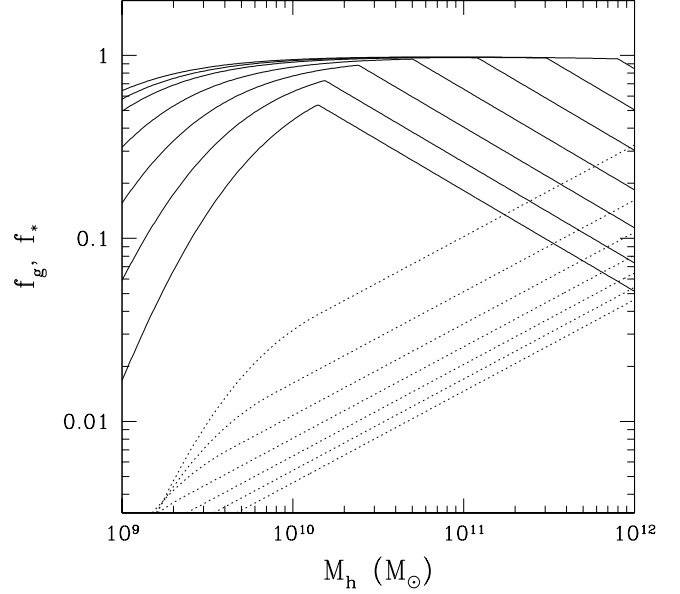


Figure 2. Same as Fig. 1, but for an alternative stellar mass prescription, eq. (9).

clusters more massive than $M_{\min} = 10^5 M_\odot$. Since we always have $M_g < f_b M_h$, in order to form even a single cluster with the minimum mass, the halo needs to be more massive than $10^9 M_\odot$. For gas-rich systems at high redshift, $M_{GC} \sim 10^{-4} M_g / f_b \sim 10^{-4} M_h$.

Given the combined mass of all clusters to be formed in an event, M_{GC} , our procedure for assigning masses to individual clusters is as follows. We first draw the most massive cluster, which we call the nuclear star cluster, even though we do not have or use the information about its actual location within the host galaxy and it is not important for our current study. The mass assigned to the nuclear cluster, M_{\max} , is derived from the assumed initial cluster mass function, $dN/dM = M_0 M^{-2}$:

$$1 = \int_{M_{\min}}^{\infty} \frac{dN}{dM} dM, \quad (11)$$

which gives $M_{\max} = M_0$. This normalization is constrained by the integral cluster mass:

$$M_{GC} = \int_{M_{\min}}^{M_{\max}} M \frac{dN}{dM} dM = M_{\max} \ln \frac{M_{\max}}{M_{\min}}. \quad (12)$$

The power-law initial mass function agrees both with the observations of young star clusters and the hydrodynamic simulations. After the nuclear cluster is drawn, the masses of smaller clusters are selected by drawing a random number $0 < r < 1$ and inverting the cumulative distribution: $r = N(< M) / N(< M_{\max})$:

$$M = \frac{M_{\min}}{1 - r (1 - M_{\min}/M_{\max})}. \quad (13)$$

We continue generating clusters until the sum of their masses reaches M_{GC} .

The formation of clusters is triggered by a gas-rich major merger of galaxies, which includes mergers of satellite halos onto the main halo as well as satellite-satellite mergers. New clusters form when the halo mass at i -th simulation output

Table 1
FIDUCIAL MODEL PARAMETERS

Parameter	Value	Effect
σ_{met}	0.1	log-normal dispersion of mass-metallicity relation
p_2	3.0	boost of the rate of cluster formation
p_3	0.2	minimum merger ratio
p_4	0.04	minimum cold gas fraction for case-1 formation
p_5	0.98	minimum cold gas fraction for case-2 formation

exceeds the mass at the previous output by a certain factor, and at the same time the cold gas fraction exceeds a threshold value:

$$\text{case-1: } M_{h,i} > (1 + p_3) M_{h,i-1} \quad \text{and} \quad f_g > p_4. \quad (14)$$

Also, we require that the maximum circular velocity does not decrease in this time step, to ensure that the mass increase was real rather than a problem with halo identification. We have experimented with a more relaxed criterion for the main halo than for satellite halos, with $p_{3,\text{main}} < p_{3,\text{sat}}$, but did not find a significantly better fit to the mass or metallicity distributions. We therefore keep a single value of p_3 for all halos.

For some model realizations, we consider an optional alternative channel for cluster formation without a detected merger, if the cold gas fraction is very high:

$$\text{case-2: } f_g > p_5, \quad (15)$$

where the threshold p_5 is expected to be close to 100%. This channel allows continuous cluster formation at high redshift when the galaxies are extremely gas-rich. High-redshift galaxies are probably in a continuous state of major and minor merging, but because of their lower masses it is more difficult to detect such mergers in the simulation. Additional motivation for this channel follows from some nearby starburst galaxies that are forming young massive clusters despite appearing isolated. Case-2 formation is allowed only for isolated halos before they are accreted into larger systems and become satellites. The epoch of accretion is defined by the last timestep before the orbit of the subhalo falls permanently within the virial radius of its host.

Our model sample combines clusters formed in the main halo and in its satellites, either surviving or disrupted. We exclude clusters from the satellites that have a galactocentric distance at $z=0$ greater than 150 kpc, which is the largest distance of a Galactic globular cluster. We apply the criteria for cluster formation at every timestep of the simulation (every $\sim 10^8$ yr) for each of the three main halos and their satellite populations. The rate of cluster formation per every merger event is therefore approximately $M_{GC}/10^8$ yr.

In order to compare the distribution of clusters obtained from our analysis to the distribution of Galactic globular clusters, we normalize the total number of model clusters by the ratio of the Galaxy mass to the simulated halo masses at $z=0$:

$$N_{\text{normalized}} = N_{\text{model}} \frac{M_{MW}}{M_{h1} + M_{h2} + M_{h3}}. \quad (16)$$

We take $M_{MW} = 10^{12} M_{\odot}$ and use $M_{h1} = 2.37 \times 10^{12} M_{\odot}$, $M_{h2} = 1.77 \times 10^{12} M_{\odot}$, and $M_{h3} = 1.70 \times 10^{12} M_{\odot}$ from Kravtsov et al. (2004).

2.3. Metallicity

The iron abundance is assigned to each model cluster according to the estimated average metallicity of its host galaxy. The latter we obtain from the mass-metallicity relation for dwarf galaxies of the Local Group at $z=0$ as formulated by Woo et al. (2008):

$$[\text{Fe}/\text{H}]_0 = -1.8 + 0.4 \log \left(\frac{M_*}{10^6 M_{\odot}} \right). \quad (17)$$

In fact, the same fit is valid for the smallest, ultrafaint dwarfs studied by Kirby et al. (2008). Thus we apply this relation to all protogalactic systems in our simulation volume.

We also include the evolution of this relation with cosmic time, based on the available observations of Lyman-break galaxies at $z \approx 2$ (Erb et al. 2006), Gemini Deep Deep Survey galaxies at $z \approx 1$ (Savaglio et al. 2005), and cosmological hydrodynamic simulations that provide the average metallicity of galaxies (Brooks et al. 2007; Davé et al. 2007):

$$[\text{Fe}/\text{H}](t) \approx [\text{Fe}/\text{H}]_0 - 0.03 \left(\frac{t_0 - t}{10^9 \text{ yr}} \right). \quad (18)$$

While this temporal evolution is probably real, it can change the metallicity for the same stellar mass by at most 0.36 dex in 12 Gyr. This amount is smaller than the 0.4 dex change of $[\text{Fe}/\text{H}]$ due to the stellar mass variation by a factor of 10. In our model, globular clusters form in protogalaxies with a range of stellar masses of several orders of magnitude (see Fig. 9 below).

The observed mass-metallicity relation for a large sample of galaxies observed by the SDSS has an intrinsic scatter of at least 0.1 dex (e.g., Tremonti et al. 2004). We account for it, as well as for possible observational errors, by adding a Gaussian scatter to our calculated $[\text{Fe}/\text{H}]$ abundances with a standard deviation of $\sigma_{\text{met}} = 0.1$ dex. The exact value of this dispersion is not important and can go up to 0.2 dex without affecting the results significantly.

Using equations (17) and (18) along with the procedures of Section 2.2, we can generate a population of star clusters with the corresponding masses and metallicities. The model contains two random factors: the scatter of metallicity and the individual cluster masses assigned via equation (13). We sample these random factors by creating 11 realizations of the model with different random seeds. Each realization combines clusters in all three main halos. Taking into account that the halos are about twice as massive as the Milky Way, the expected number of clusters in each model realization is ~ 150 (the observed number) $\times (2.37 + 1.77 + 1.7) \approx 870$. The total set of all 11 realizations includes ~ 9500 clusters. For the purpose of conducting statistical tests on the distributions of cluster mass and metallicity, we consider each realization separately and then take the median value of the calculated statistic.

For convenience, we provide a list of the most important equations we used in the model in table 2.

3. DYNAMICAL DISRUPTION

Star clusters are prone to gradual loss of stars, and in some cases, total disruption by internal and external processes. It is expected that the mass function of globular clusters has evolved through cosmic time, from an initial (probably, a power law) distribution to the approximately log-normal distribution that is observed today. Since the main focus of this

Table 2
SUMMARY OF MODEL EQUATIONS

Equation	Section	Description
2	2.1	fraction of baryons accreted onto a halo
3	2.1	cutoff mass for baryon accretion
5	2.1	cold gas mass relative to stellar mass
7	2.1	stellar mass relative to halo mass
10	2.2	mass in globular clusters relative to gas mass
17	2.3	stellar mass-metallicity relation for halos
24	3	evolution of cluster mass

paper is on the observable properties of the Galactic population, we evolve all of our model clusters dynamically from their time of formation until the present epoch. We adopt the evaporation via two-body relaxation and stellar evolution as the mechanisms for mass loss. Tidal shocks are ignored for simplicity. Cluster mass changes because of the decrease of the number of stars, $N_*(t)$, by evaporation and the decrease of the average stellar mass, $\bar{m}(t)$, by stellar evolution:

$$\frac{1}{M} \frac{dM}{dt} \equiv \frac{1}{N_*} \frac{dN_*}{dt} + \frac{1}{\bar{m}} \frac{d\bar{m}}{dt} = -\nu_{\text{ev}}(M) - \nu_{\text{se}}(t) \frac{\bar{m}(0)}{\bar{m}}. \quad (19)$$

We have assumed, as done in the recent literature, that the evaporation rate depends only on cluster mass. The time t for each cluster is measured from the moment of its formation.

We adopt the calculation of Prieto & Gnedin (2008) for the time-dependent mass-loss rate due to stellar evolution, $\nu_{\text{se}}(t)$ (see their Fig. 7). That calculation uses the relation between star's initial mass and remnant mass from Chernoff & Weinberg (1990) and the main-sequence lifetimes from Hurley et al. (2000). Over time, stellar evolution reduces the cluster mass by up to 40%, for a Kroupa (2001) IMF. This implies that no clusters are disrupted by stellar evolution alone, and the net effect is only a shift in the mass distribution towards the lower end.

We now need to derive the evaporation rate, $\nu_{\text{ev}}(M)$, as a function only of cluster mass. We begin by writing down the standard approximation (Spitzer 1987) using the half-mass relaxation time, t_{rh} :

$$\nu_{\text{ev}} = \frac{\xi_e}{t_{rh}} = \frac{7.25 \xi_e \bar{m} G^{1/2} \ln \Lambda}{M^{1/2} R_h^{3/2}}, \quad (20)$$

where ξ_e is the fraction of stars that escape per relaxation time, R_h is the half-mass radius, and $\ln \Lambda$ is the Coulomb logarithm. We take $\bar{m} = 0.87 M_\odot$ for a Kroupa IMF, and $\ln \Lambda = 12$, which is a common value used for globular clusters (Spitzer 1987).

We then assume that at the time of formation R_h depends only on cluster mass, as $R_h \propto M^{\delta_0}$, and not on the position in the host galaxy. As a fiducial model, we use a constant density model where $\delta_0 = 1/3$ (Kravtsov & Gnedin 2005; Prieto & Gnedin 2008). The relation for the initial size is normalized with respect to the median observed mass of Galactic clusters, $2 \times 10^5 M_\odot$, and their median size of 2.4 pc:

$$R_h(0) = 2.4 \text{ pc} \left(\frac{M(0)}{2 \times 10^5 M_\odot} \right)^{\delta_0}. \quad (21)$$

A similar relation extends to other dynamically hot stellar systems: nuclear star clusters and ultracompact dwarf galaxies (Kissler-Patig et al. 2006). The mass-size relation may

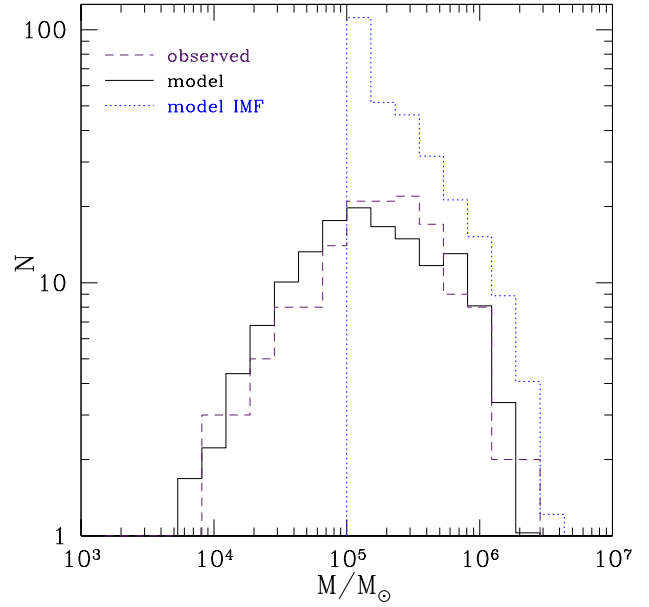


Figure 3. Dynamically evolved clusters at $z = 0$ in the fiducial model with $\xi_e = 0.033$, $\delta = \delta_0 = 1/3$ (solid histogram), compared to the observed distribution of Galactic globular clusters (dashed histogram). Dotted histogram shows the combined initial masses of model clusters formed at all epochs, including those that did not survive until the present. In the model we do not follow clusters with the initial masses below $10^5 M_\odot$.

change over the course of the cluster evolution. We consider a power-law relation with a potentially different slope, so that the half-mass radius responds to changes in the cluster mass as

$$\frac{R_h(t)}{R_h(0)} = \left(\frac{M(t)}{M(0)} \right)^\delta. \quad (22)$$

Our preferred value is again $\delta = 1/3$, but we also discuss results for other choices of δ_0 and δ . Recent N -body models of cluster disruption are consistent with $\delta \approx 1/3$ (Trenti et al. 2007; Hurley et al. 2008). Note that cluster sizes are only used as an intermediate step in the derivation of $\nu_{\text{ev}}(M)$ and can be subsequently ignored. The evaporation time thus becomes

$$\nu_{\text{ev}}^{-1} \approx 10^{10} \text{ yr} \left(\frac{\xi_e}{0.033} \right)^{-1} \left(\frac{M(0)}{2 \times 10^5 M_\odot} \right)^{\frac{1+3\delta_0}{2}} \left(\frac{M(t)}{M(0)} \right)^{\frac{1+3\delta}{2}}. \quad (23)$$

The fraction ξ_e is not well constrained. The lower limit on ξ_e is achieved in isolated clusters, for which $\xi_e = 0.0074$ (Ambartsumian 1938; Spitzer 1940). Tidally-truncated clusters lose stars at a faster rate, as first calculated by Hénon (1961) and Spitzer & Chevalier (1973). Using orbit-averaged Fokker-Planck models of cluster evolution, Gnedin et al. (1999) found ξ_e varying between 0.02 and 0.08 depending on time and cluster concentration (their Fig. 4 and Table 2). More recently, realistic direct N -body models became possible (e.g., Baumgardt 2001; Baumgardt & Makino 2003). These calculations revealed that the gradual escape of stars through the tidal boundary, which is not spherical as in the Fokker-Planck calculations, breaks the linear scaling of the disruption time with the relaxation time. Baumgardt (2001) suggested that the evaporation time scales as $\nu_{\text{ev}}^{-1} \propto t_{rh}^{3/4}$. Gieles & Baumgardt (2008) verified this relation and found almost no dependence on the cluster half-mass radius. In-

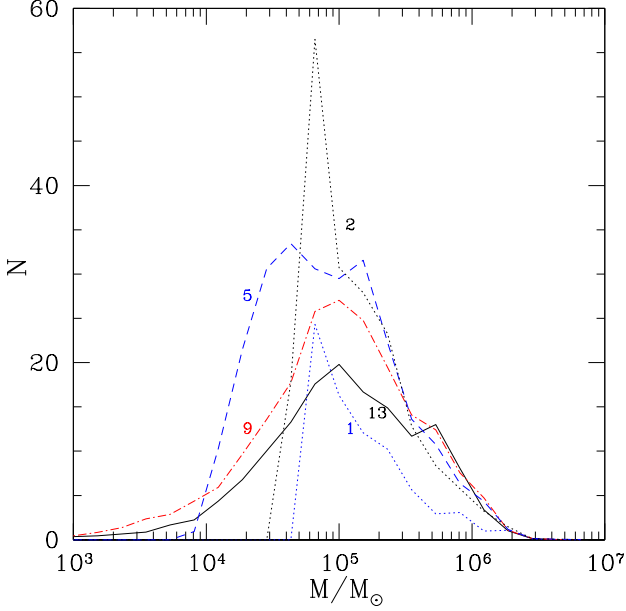


Figure 4. The mass function of clusters in the fiducial model at different epochs corresponding to the cosmic times of 1 Gyr ($z \approx 5.7$, dotted), 2 Gyr ($z \approx 3.2$, dotted), 5 Gyr ($z \approx 1.3$, dashed), 9 Gyr ($z \approx 0.5$, dot-dashed), and 13.5 Gyr ($z = 0$, solid).

stead, they proposed an explicit dependence on the Galactocentric distance R_G and velocity V_G , to reflect the strength of the local tidal field: $\nu_{\text{ev}}^{-1} \propto \omega^{-1} \equiv R_G/V_G$. This gives $\nu_{\text{ev}}^{-1} \propto M^{3/4} \omega^{-1}$. Their formula is similar to the empirical estimates of the disruption time by Lamers et al. (2005): $\nu_{\text{ev}}^{-1} \propto M^{0.65}$.

Since the calculation of the local tidal field is currently beyond our simple model, we ignore the dependence on the Galactocentric distance but argue that we can incorporate the result of Gieles & Baumgardt (2008) for the disruption timescale by using a lower value of $\delta_0 = \delta = 1/9$. With this choice of the exponents, our equation (23) gives $\nu_{\text{ev}}^{-1} \propto M^{2/3}$. We discuss these alternative models in Section 4.6.

For consistency with Prieto & Gnedin (2008), we adopt $\xi_e = 0.033$ for the fiducial model.

With the above ingredients, we can now compute the cluster mass at time t after formation by inverting $\nu_{\text{ev}}(M)$ in equation (19) and assuming that most of the stellar evolution mass loss happens much faster than the evaporation:

$$M(t) = M(0) \left[1 - \int_0^t \nu_{\text{se}}(t') dt' \right] \left[1 - \frac{1+3\delta}{2} \nu_{\text{ev},0} t \right]^{2/(1+3\delta)}, \quad (24)$$

where $\nu_{\text{ev},0} \equiv \nu_{\text{ev}}(M = M(0))$.

The initial mass function of globular clusters is evolved from the time of formation until the present epoch and is shown in Figure 3 for the fiducial model. The observed mass function in the Milky Way is well represented by a log-normal distribution. We derive the masses of the Galactic clusters by taking their absolute V-band magnitudes from the Harris (1996) catalog and assuming a constant mass-to-light ratio $M/L_V = 3 M_\odot/L_\odot$. The functional form of a Gaussian built around $\log M$ for the observed sample is given by

$$\frac{dN}{d \log M} = \frac{1}{\sqrt{2\pi}\sigma_M} \exp \left[-\frac{(\log M - \overline{\log M})^2}{2\sigma_M^2} \right], \quad (25)$$

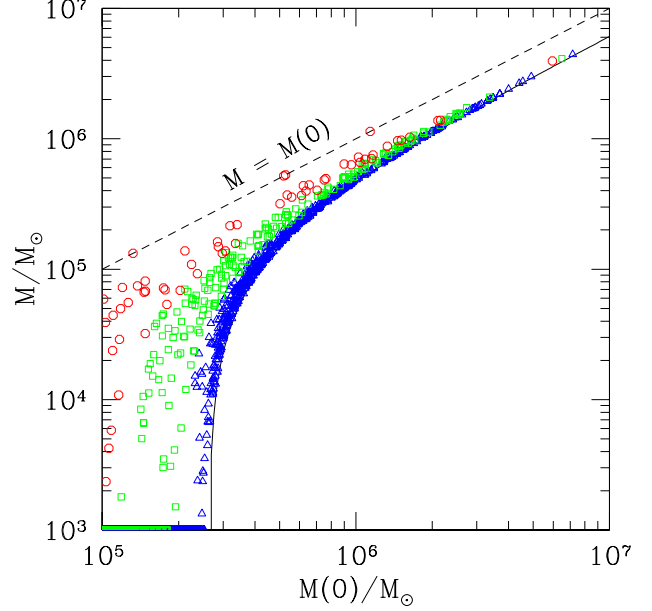


Figure 5. Final mass of model clusters vs. their initial mass, for a single realization of the fiducial model. Clusters are divided into three age groups: triangles represent old clusters (age > 10 Gyr), squares represent intermediate age clusters ($5 \text{ Gyr} < \text{age} < 10 \text{ Gyr}$), and circles represent young clusters (age < 5 Gyr). All disrupted clusters are placed at the bottom of the plot, to illustrate the range of their initial mass. The birthline of clusters, $M = M(0)$, is plotted as a dashed line for reference.

with the mean $\overline{\log M} = 5.22$ and standard deviation $\sigma_M = 0.61$, in solar masses. The predicted mass function in the fiducial model with $\xi_e = 0.033$ and $\delta = \delta_0 = 1/3$ is consistent with the observations. The Kolmogorov-Smirnov (KS) test probability of the two mass functions being drawn from the same distribution is $P_{KS,M} = 7.4\%$. This value is the median of the KS probabilities for the 11 random realizations of the model. The model distribution is also well fit by a Gaussian, with $\overline{\log M} = 5.14$ and $\sigma_M = 0.65$.

The mean of the model distribution is slightly lower than observed, implying that the disruption process needs to be stronger to fully reconcile with the data. Clusters that start out with low mass but are not disrupted effectively over their lifetime over-populate the low end of the present-day model mass function. Old and intermediate-age clusters that started with initial mass $5 < \log M < 5.4$ and survived until the present era appear to be the main cause of this discrepancy.

Figure 4 illustrates the evolution of the mass function over cosmic time as an interplay between the continuous buildup of massive clusters ($M > 10^5 M_\odot$) and the dynamical erosion of low-mass clusters ($M < 10^5 M_\odot$). Since we do not track the formation of clusters below M_{min} , the low end of the mass function was built by a gradual evaporation of more massive clusters. The strongest bout of cluster formation happens between a cosmic time of 1 and 5 Gyr, and a peak of the mass function forms at $M \sim 3 \times 10^4 M_\odot$. The peak moves to larger masses, $\sim 10^5 M_\odot$ by $t = 9$ Gyr, while a power-law tail develops at low masses. A significant fraction of low-mass clusters is disrupted between 9 Gyr and the present, as few new clusters are produced.

The relation between the cluster initial and final masses is shown in Figure 5. Old clusters that have undergone significant amounts of dynamical and stellar evolution form a

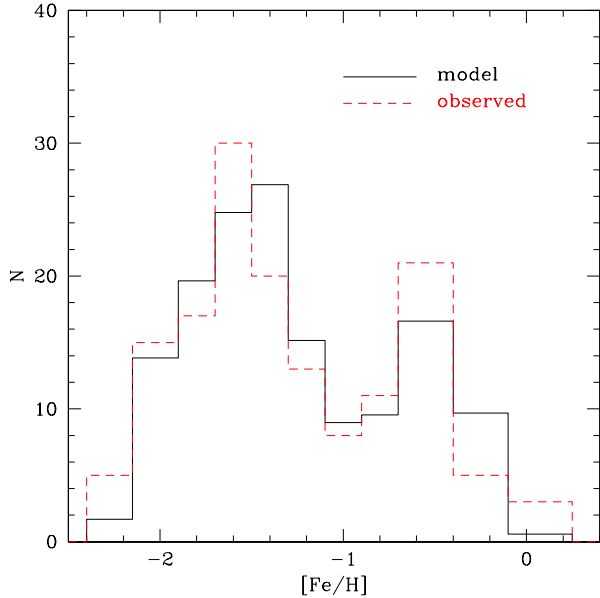


Figure 6. Metallicities of model clusters formed at all epochs that have survived dynamical disruption by $z = 0$ in the fiducial model (*solid histogram*), compared to the observed distribution of Galactic globular clusters (*dashed histogram*).

tight sequence on this plot. The lower boundary with a dense concentration of points corresponds to the expression $M = 0.63 [M(0) - 2.6 \times 10^5 M_\odot]$, which reflects 13 Gyr of stellar and dynamical evolution according to equation (24) with the fiducial values of the parameters. Thus an old cluster must have an initial mass of at least $2.6 \times 10^5 M_\odot$ to survive dynamical disruption. Clusters in the younger age groups fill the space between their birthline and this boundary. The youngest clusters have the shallowest slope at low mass, as few of them have had enough time to undergo significant disruption. The mean final mass for all three age groups is about the same, implying that some of the oldest globular clusters could have been more massive at the time of their formation than clusters that have formed recently in the local universe.

Fall & Zhang (2001) suggested that a low-mass end of the mass function should approach $dN/dM \approx \text{const}$ as a result of dominant disruption by two-body evaporation. Our mass function in the range $3.5 < \log(M/M_\odot) < 5.0$ is consistent with a power law $\log(dN/d \log M) = 0.89 \log M - 3.04$, or $dN/dM \propto M^{-0.11}$, in good agreement with the expectation.

4. RESULTS

4.1. Exploration of the Parameter Space

Overall, our model has five adjustable parameters (Table 1). To explore possible degeneracies among these parameters, and to find the parameter set that produces the best-fitting metallicity distribution, we set up a grid of models in which each of the parameters was varied within a finite range of values. The range was taken to be large enough to explore all physically relevant values of each parameter.

The boost for cluster formation, p_2 , varied from 0 to 5. For consistency with the rate derived in the hydrodynamic simulation of Kravtsov & Gnedin (2005), we aimed to keep this parameter at low values.

The minimum mass ratio for mergers, p_3 , varied between 0.15 and 0.5. It is consistent with typical major merger criteria

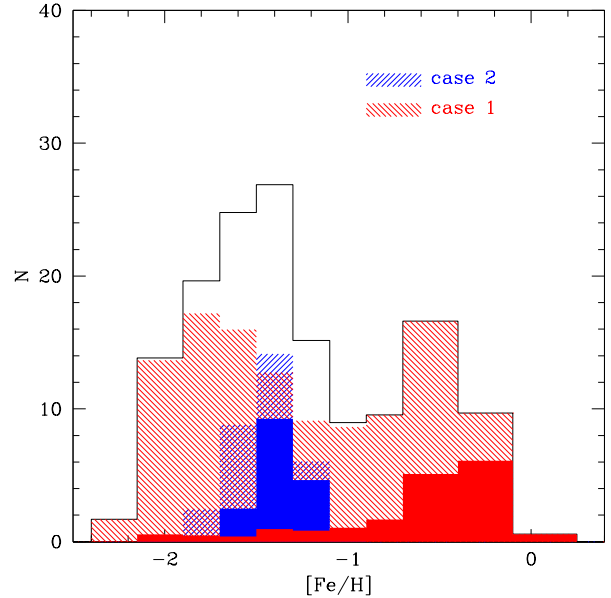


Figure 7. Metallicity distribution in the fiducial model, split by the formation criterion: major mergers (*case-1*) and early mergers (*case-2*). Solid histograms show the clusters formed in the main Galactic halo.

used in the literature (e.g. Beasley et al. 2002 use $p_3 = 0.3$).

The cold gas fraction required for cluster formation during a merger, p_4 , could be relatively low but non-zero, so that we considered $0 < p_4 < 0.2$. This threshold parameter accounts for why disk galaxies like the Milky Way are still forming stars despite a low gas fraction, while ellipticals are not.

The gas fraction for *case-2*, p_5 , has to be very high – above 90%, as our prescription predicts that many halos have a very high gas fraction at high redshift and could over-produce blue globular clusters (as was the case in the Beasley et al. 2002 model).

We considered several values for σ_{met} but found that a value of 0.2 or higher smeared out the peaks in the metallicity distribution, while a value of 0 failed to fill the extreme ends of the distribution. We therefore include only three values in our search, $\sigma_{\text{met}} = 0, 0.1, 0.2$.

We find the best-fit model by searching through the multi-parameter space and maximizing the KS probabilities of the metallicity distribution, $P_{KS,Z}$, and the mass function, $P_{KS,M}$, being consistent with observations. The likelihood function also contains additional factors that force the parameters towards the values that we consider ideal. We require the model to produce the observed number of clusters, $N \approx 150$, scaled by the host galaxy mass as in equation (16). We wish to maximize the fraction of clusters formed in the main disk, f_{disk} , to be consistent with the observed spatial distribution (Section 5). We penalize the likelihood function for large values of p_2 and for any young clusters formed after $t = 10$ Gyr, $N_{\text{after}10}$. We also wish to minimize the fraction of clusters formed through the *case-2* channel, $f_{\text{case}2}$, for simplicity of the model. Finally, we want to increase the likelihood of the metallicity distribution being bimodal, as characterized by the Dip test, P_{dip} , which we discuss later in Section 4.4. The actual likelihood function that we maximize is given by

$$\log \mathcal{L} = \log P_{KS,Z} + 0.3 \log P_{KS,M} - [(N - 150)/30]^2 + \log f_{\text{disk}} - 0.15 p_2 - 20 N_{\text{after}10}/N - 0.4 f_{\text{case}2} + 3 \log P_{\text{dip}}. \quad (26)$$

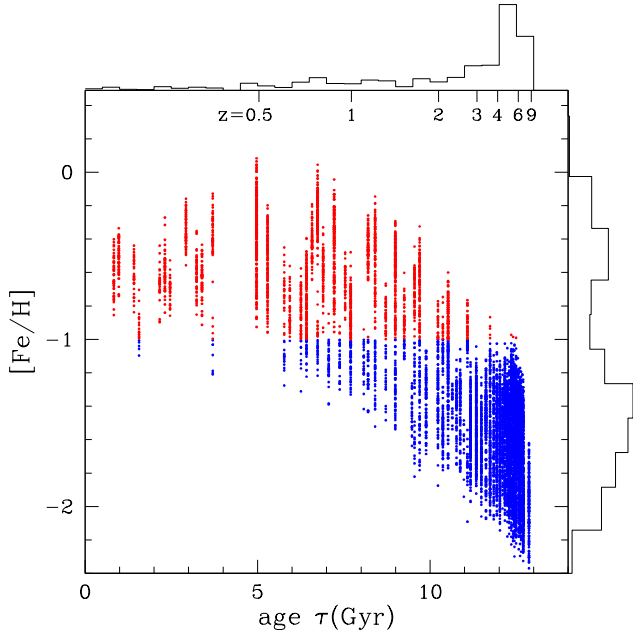


Figure 8. Age-metallicity relation in all 11 realizations of the fiducial model (≈ 9500 clusters). The build-up of massive halos drives the steep slope of this relation at early epochs. Outer histograms show marginalized distributions on linear scale. Notice an order-of-magnitude spread in metallicities of clusters forming at a given epoch.

The coefficients for each term were adjusted heuristically until we found that their relative weights matched our expectation to select acceptable distributions. The “best-fit” distribution that maximizes \mathcal{L} is therefore a subjective fiducial model that we use to illustrate how the bimodality may arise. We then look at how many model realizations are similar to the “best-fit” for other possible values of the parameters.

4.2. Age and Metallicity Distributions

Figure 6 shows the predicted best-fit metallicity distribution of model clusters and the observed distribution of Galactic globular clusters, both metal-poor and metal-rich. Note that we require our model to have the same formation criteria for both cluster populations; we do not explicitly differentiate between the two modes. The only variable is the gradually changing amount of cold gas available for star formation. Yet, the model predicts two peaks of the metallicity distribution, centered on $[\text{Fe}/\text{H}] = -1.54$ and $[\text{Fe}/\text{H}] = -0.58$, in remarkable agreement with the observations. The standard deviation of the red peak is 0.24 dex and of the blue peak is 0.32 dex.

The probability of KS test of the model and data samples being drawn from the same distribution is $P_{KS,Z} = 80\%$, that is, they are fully consistent with each other. The number of surviving clusters is $N = 147$, also matching the observations. Even though our current model is extremely simple, this bimodality is reproduced naturally, without explicit assumptions about truncation of the production of metal-poor clusters at some early epoch or about the formation of metal-rich clusters in a merger of two spiral galaxies.

We find that the main halo contributes more significantly to the red peak than it does to the blue peak (Figure 7). In particular, clusters with the highest $[\text{Fe}/\text{H}]$ appear to have been formed primarily by late merging into the main halo.

The fraction of clusters formed via case-2 channel is $f_{\text{case2}} = 22\%$. These clusters produce a single-peaked distri-

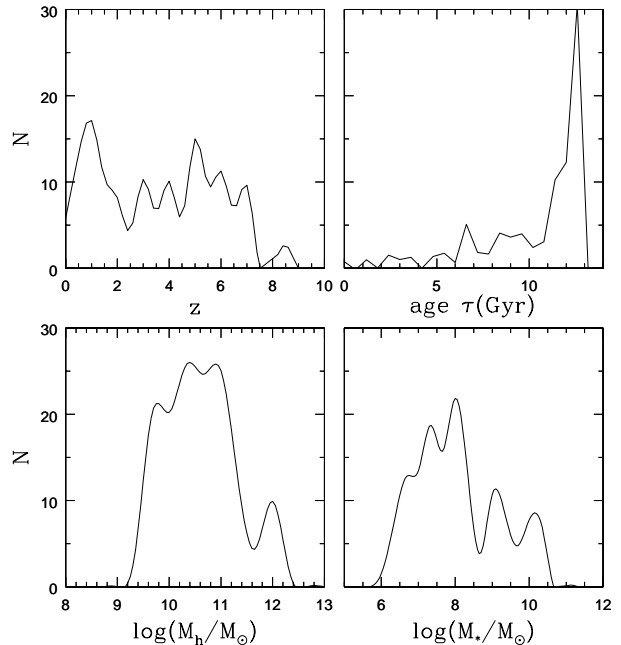


Figure 9. Number of clusters in the fiducial model as a function of the environment: redshift of formation (*top left panel*), present age (*top right panel*), host halo mass at the time of formation (*bottom left panel*), and host stellar mass (*bottom right panel*).

bution of blue clusters. In contrast, clusters formed in major mergers contribute to both red and blue modes, in about equal proportions. We return to this point in the discussion of globular cluster systems of elliptical galaxies in Section 7.

Clusters that formed after $z = 2$ constitute the bulk of the red peak and contribute little to the blue peak in the metallicity distribution (Figure 8). The strength of this result implies that the gas reservoir and the rate of hierarchical merging at intermediate redshifts is conducive to the creation of red clusters. This result lends itself well to the idea that the simulation of Kravtsov & Gnedin (2005) was only able to reproduce the metal-poor population of globular clusters because the simulation was stopped at $z \approx 3$.

Our prescription links cluster metallicity to the average galaxy metallicity in a one-to-one relation, albeit with random scatter. Since the average galaxy metallicity grows monotonically with time, clusters forming later have on the average higher metallicity. The model thus encodes an age-metallicity relation, in the sense that metal-rich clusters are younger by several Gyr than their metal-poor counterparts. This relation is required in the model to reproduce the observed metallicity distribution, because very old galaxies cannot produce high enough metallicities. However, Figure 8 shows that clusters of the same age may differ in metallicity by as much as a factor of 10, as they formed in the progenitors of different mass.

Available observations of the Galactic globular clusters do not show a clear age-metallicity relation, but instead indicate an age spread increasing with metallicity (De Angeli et al. 2005; Marín-Franch et al. 2009; Dotter et al. 2010; Forbes & Bridges 2010). Red clusters have younger mean age overall and may be as young as $\tau \approx 7$ Gyr. Our model does not appear to be in an obvious conflict with this trend. We define cluster age as $\tau \equiv t_0 - t_f$, where t_f is the time of formation. We find the mean age of 11.7 Gyr for the blue population and 6.4 Gyr for the red population, with the

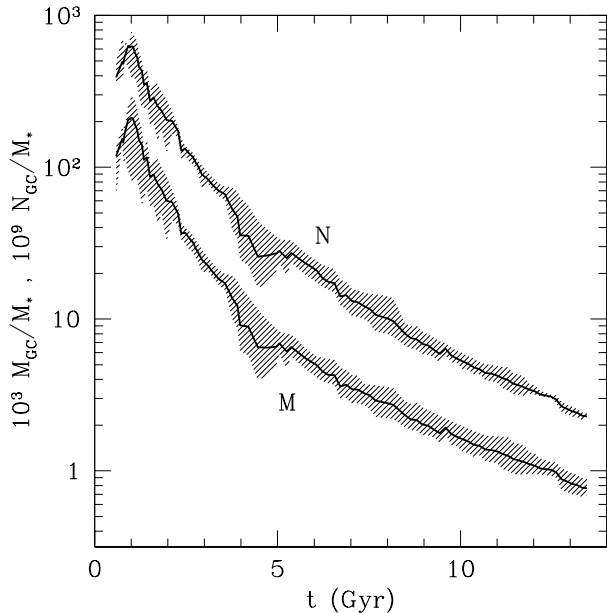


Figure 10. Ratios of total cluster mass and number to the galaxy stellar mass, summed over all systems that are located within 150 kpc of the center at $z = 0$. Lines represent the average over all three host halos and their corresponding subhalo populations. Shading represents the scatter in these ratios, given by the lowest and highest values among the three hosts. Massive star cluster formation was a much more dominant component of galactic star formation at early times than it has been for the last 10 Gyr.

standard deviation of 1.3 Gyr and 2.7 Gyr, respectively. More accurate dating of the Galactic and extragalactic clusters is needed to falsify the predicted age-metallicity trend.

Distributions of the cluster formation time and environment in the fiducial model are shown in Figure 9. The age distribution, which peaks strongly between 11 and 13 Gyr, demonstrates that the majority of our clusters is still very old and falls in line with the observed perception of globular clusters. However, the distribution of formation redshift appears remarkably flat in the range $1 < z < 7$, emphasizing that the clusters were not formed in a single event but rather through the continuous process of galaxy formation. Few clusters were formed prior to the era of reionization, as sufficiently large quantities of gas could not be condensed to meet the mass threshold for cluster formation at redshifts $z > 9$. The distributions of the total and stellar mass of the host galaxies extend over three orders of magnitude. Their extended high-mass tails contribute to the strength of the red peak, as the most massive halos would form most metal-rich clusters.

Globular clusters form much earlier than the majority of field stars. Figure 10 shows the fraction of galaxy stellar mass locked in massive star clusters, normalized for convenience as $10^3 M_{GC}/M_*$. To calculate this ratio, we summed over all protogalactic systems that would end up within 150 kpc of the galaxy center at $z = 0$, regardless of their location at earlier times. Thus it represents a global cluster formation efficiency in a Milky Way-sized environment. Specific realizations of the model differ in detail in the three host halos, by as much as a factor of 2. This scatter is shown by the shaded region on the plot. The globular cluster mass includes their continuous formation and the mass loss due to the dynamical evolution. A striking prediction of the model is a very high cluster fraction at early times, near $t = 1$ Gyr, of $M_{GC}/M_* \approx 10\text{--}20\%$.

Star cluster production may have been a dominant component of galactic star formation at $z > 3$. By $t = 3$ Gyr ($z \approx 2$), the cluster fraction drops to only a few percent, as expected for a galaxy undergoing active star formation. At the current epoch, massive star clusters make up less than 0.1% of the stellar mass. The predicted ratio is progressively more uncertain at higher redshift because it relies on our extrapolated prediction for the galactic stellar mass. The low-redshift prediction should be robust. We also show a variant of the specific frequency parameter related to the number of clusters, $T \equiv N/(M_*/10^9 M_\odot)$, introduced by Zepf & Ashman (1993). It shows a similar decline with time, reaching $T \approx 2$ at the present.

These global cluster formation efficiencies agree with many observations across galaxy types. Rhode et al. (2005) find $T \sim 1$ for both red and blue clusters in the field and group spiral galaxies. This parameter increases with the galaxy mass. In the Virgo cluster, Peng et al. (2008) find $T \sim 5$ for galaxies in the mass range appropriate for the Milky Way. McLaughlin (1999) estimated the cluster mass fraction in both spiral and elliptical galaxies to be $M_{GC}/(M_* + M_g) \approx 0.0026 \pm 0.0005$. This is larger than what we find by a factor of several, but we count in M_* all stars out to 150 kpc, which includes some satellite galaxies as well as the host. Therefore, both predicted cluster efficiencies at $z = 0$ are reasonable. Their rise at high redshift is an interesting prediction of the model.

The model also shows that the globular cluster system overall is more metal-poor than the stars in disrupted satellites, which are expected to form a stellar spheroid of the Galaxy. We calculated the mass-weighted metallicity of stars formed in the disrupted satellites of all three main halos (using eqs. 7, 8, 17, 18). This calculation bears all the uncertainty of our extrapolated time evolution of the stellar fraction and mass-metallicity relation, but nevertheless provides a useful estimate. We find the tail of halo star metallicities as low as the most metal-poor globular clusters, but the overall stellar distribution peaks around $[\text{Fe}/\text{H}] \approx -0.3$. A very similar situation is observed in NGC 5128 and discussed by Harris (2010). In our model, majority of globular clusters form before the bulk of field stars and therefore acquire lower metallicities. For comparison, the metallicity of stars in surviving satellite galaxies peaks around $[\text{Fe}/\text{H}] \approx -0.8$ and forms an intermediate population between the clusters and the field.

Despite our attempts to incorporate it as a major penalty in the likelihood statistic, we were unable to completely eliminate the phenomenon of young massive star clusters. Interestingly, these clusters did not originate in the main galactic disks. All clusters younger than 5 Gyr formed in satellite halos in the mass range $\sim 10^{10} - 10^{11} M_\odot$, at distances 40–100 kpc from the center. Although the proper sample of the Galactic globular clusters does not contain any young clusters, there are several young massive clusters in M31 whose ages were confirmed both from the visual and UV colors (Fusi Pecci et al. 2005; Rey et al. 2007) and from the integrated-light spectroscopy (Puzia et al. 2005). The actual analogs of young model clusters may be found in the LMC, which hosts globular clusters with a wide range of ages and continues to form clusters now. There may even exist young star clusters with masses $\sim 10^5 M_\odot$ in the Galactic disk, hidden behind tens of visual magnitudes of extinction but revealing themselves through free-free emission of their ionization bubbles (Murray & Rahman 2010). Massive star cluster formation at late times thus paints a picture consistent with the

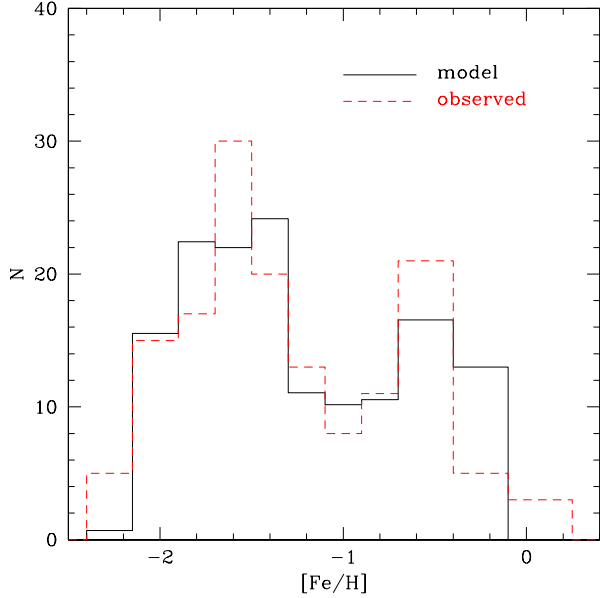


Figure 11. Metallicity distribution at $z=0$ in the model without *case-2* formation (solid histogram), compared to the observed distribution of Galactic globular clusters (dashed histogram).

idea that today’s super star clusters are destined to become observationally equivalent to globular clusters, as envisioned by Ashman & Zepf (1992) and Harris & Pudritz (1994).

A separate criterion for the formation of clusters in extremely gas-rich systems (*case-2*) is not necessary for achieving a good fit to the observed metallicity distribution. Though we feel that the inclusion of *case-2* formation channel in the model is both useful and physically motivated, it takes away from the elegance of using only resolved mergers as a lone formation mechanism. It turns out that the main benefit of allowing clusters to form via *case-2* is seen in the mass function of surviving clusters. The high-mass end of the mass function matches the observations better if massive halos (primarily the main halo) are allowed to form as many clusters as possible at early times.

We searched the model grid without *case-2*, by setting $p_5 = 1$, and found an almost equally good metallicity distribution as in the fiducial model. Figure 11 shows that this distribution also appears bimodal and completely consistent with the data. The KS probability is $P_{KS,Z} = 92\%$. In fact, even the mass function is only marginally less consistent, $P_{KS,M} = 2.0\%$ vs. 7.4% in the fiducial model. The parameters used to obtain this distribution were: $p_2 = 2.85$, $p_3 = 0.16$, $p_4 = 0.04$, $p_5 = 1$, $\sigma_{\text{met}} = 0.1$.

4.3. Sensitivity to Model Parameters

The fiducial distribution discussed above is not unique among our results in its ability to match the observations. Significant degeneracy exists among combinations of the model parameters that produce metallicity distributions consistent with the Galactic sample. Many models within the grid have sufficiently high KS probabilities. In this section we explore which regions of the parameter space produce models similar to our best fit.

First, let us motivate the use of the likelihood function given by equation (26) as opposed to using a standard statistical test

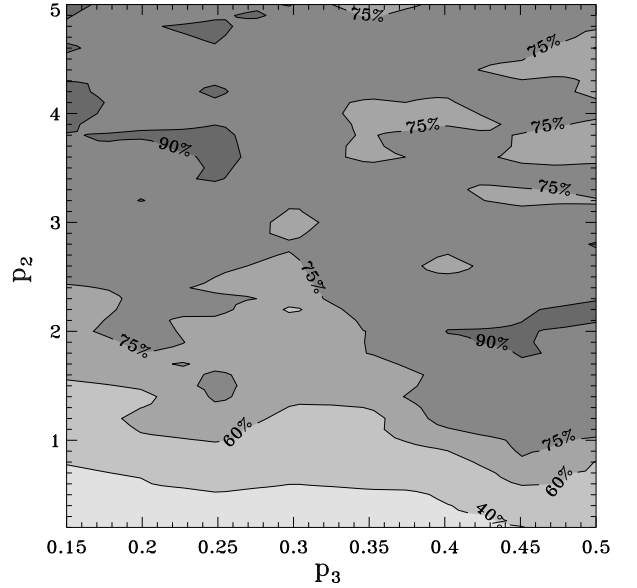


Figure 12. Contour plot of the KS probability for the metallicity distributions in the plane of parameters $p_2 - p_3$. Contour labels are the actual probability values, $P_{KS,Z}$. This plot shows that KS test alone cannot rule out any region of the parameter space from being statistically consistent with the data.

to select the best fit. In the early stages of development of our model, we relied on KS test alone to help us understand the range of parameters that produce metallicity distributions that match the observations. However, once the model was completed, it became apparent that KS test alone was not powerful enough for analysis of the results. This is clearly demonstrated in Figure 12, which shows the value of the KS probability $P_{KS,Z}$ as a function of p_2 and p_3 across their respective ranges in the grid. Each point represents the maximum possible $P_{KS,Z}$ for the given values of p_2 and p_3 with the other parameters free to vary within the grid. This is done to best represent the full extent of the 5-dimensional parameter space within a 2-dimensional slice. Statistically, any distribution with $P_{KS,Z} > 10\%$ cannot be ruled out with confidence, implying that almost the entire range of our parameters can produce statistically consistent distributions! In addition, although some regions of the parameter space have higher values of $P_{KS,Z}$ than others, there is no clear pattern in the contours to help us understand the required physics of star cluster formation within our semi-analytical recipe.

In comparison, Figure 13 shows contours of the value of the likelihood function from equation (26), using the same scheme described above to maximize the value at each point. The shape of these contours demonstrates that p_2 and p_3 are degenerate in their ability to produce good distributions. The degeneracy can most easily be understood by noting that these parameters directly affect the total number of clusters: p_2 controls the cluster formation rate per merger, while p_3 selects eligible mergers. It is therefore expected that the contours show a correlation at high levels of the likelihood function, as the statistic depends sensitively on the total number of clusters.

Figure 14 shows the same type of contours as Fig. 13, but only for distributions with $p_5 = 1$. Disallowing the *case-2* channel reduces the range of the parameter space where good distributions are found. In particular, compared to the previous plot, Fig. 14 lacks any viable models with $p_3 > 0.3$. Given

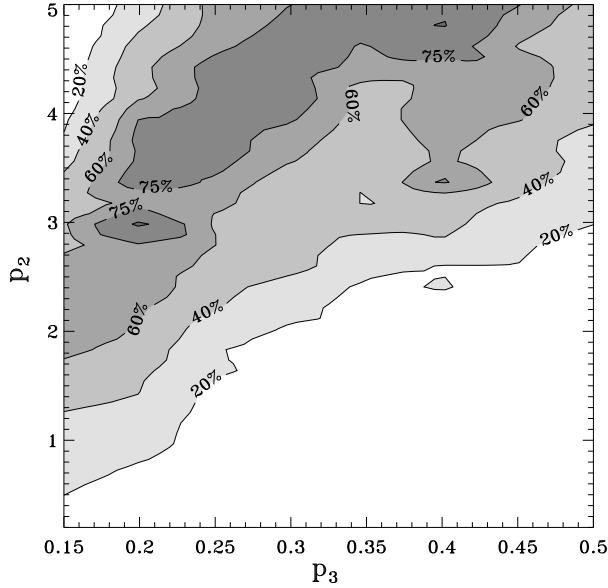


Figure 13. Contour plot of the likelihood statistic \mathcal{L} in the plane of parameters $p_2 - p_3$. Contour labels show percentages of the maximum. The highest-value region is a degeneracy along the line $p_2 = 19p_3 - 0.91$.

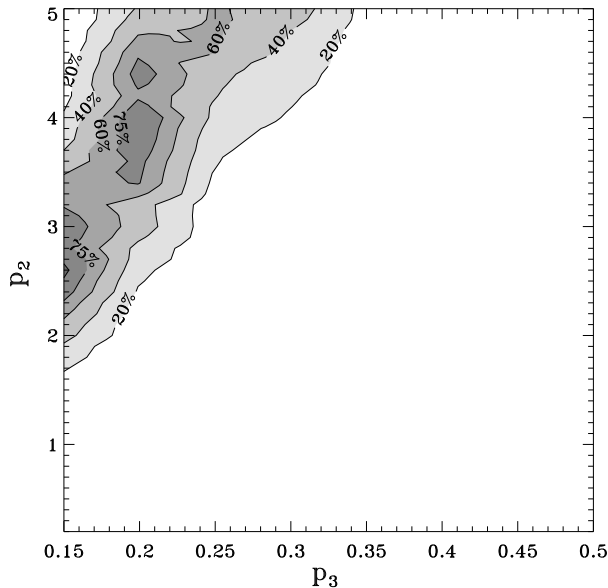


Figure 14. Same as Figure 13 but for the models without *case-2*. The highest-value region is a degeneracy along the line $p_2 = 24p_3 - 1.1$.

the tight and steep correlation in this plot, it is likely that larger values of p_3 would require very high $p_2 > 5$, which may violate current observational constraints on the cluster formation efficiency. However, Fig. 11 demonstrates that a good model can still be found with reasonably small values of p_2 and p_3 , without the *case-2* channel.

To understand the sensitivity of the likelihood function to individual parameters, we also considered one-dimensional slices of the parameter space around the fiducial model, this time allowing for only one parameter to vary at a time. Figure 15 illustrates how the sharp peaks of \mathcal{L} allow us to se-

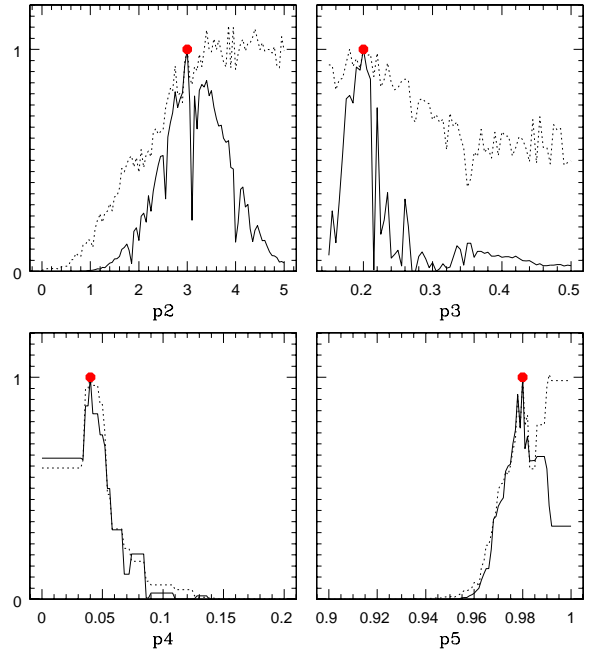


Figure 15. Marginalized single-parameter likelihood distributions around the fiducial model, $\mathcal{L}/\mathcal{L}_{\max}$ (solid lines). Dashed lines show the metallicity probability $P_{KS,Z}$ normalized to the fiducial model value. Compared with $P_{KS,Z}$ alone, the likelihood function \mathcal{L} significantly tightens the constraints on the best values of the parameters. Filled circles show the fiducial model.

lect the best model more accurately than on the basis of $P_{KS,Z}$ alone. Particularly as a function of p_2 and p_3 , $P_{KS,Z}$ varies slowly over the entire range of the grid. On the other hand, p_4 and p_5 must stay within a small range of their fiducial values in order to achieve acceptable values of either $P_{KS,Z}$ or \mathcal{L} .

Figure 16 shows variation of the metallicity distribution when individual parameters deviate from their fiducial values. Each parameter can change the shape of the metallicity function and the number of clusters. The effects of varying p_2 and p_3 are almost opposite, reflecting the degeneracy in the likelihood contours. In particular, smaller p_3 accommodates more minor mergers, which allow massive hosts form more metal-rich clusters as well as some metal-poor clusters. Decreasing p_5 allows more clusters form through the *case-2* channel; most of such clusters are metal-poor. The major role of p_4 appears to govern the extent of the most metal-rich clusters – lower threshold gas fraction allows clusters to form in the later, more enriched environments of massive hosts.

Figure 17 illustrates the response of the metallicity distribution to simultaneous variations of model parameters. First, we plot two distributions where we changed p_3 to 0.15 and 0.3 while keeping the other parameters fixed. The width of the metal-poor peak broadens as p_3 is lowered, indicating that a wider range of halos in the early universe were able to produce clusters. Raising p_3 has the opposite effect. Note that the locations of the two peaks are remarkably robust to these changes. Staying at $p_3 = 0.15$, we set $p_5 = 1$ to eliminate the *case-2* channel and set $p_4 = 0$ to allow even gas-poor massive halos at low redshift to form clusters. The result (long-dashed line) is a distribution with a much broader metal-rich peak, which extends well past the maximum metallicity of the fiducial model. The dot-dashed line represents a corresponding change to $p_4 = 0.08$ and $p_5 = 0.96$ for the $p_3 = 0.3$ model.

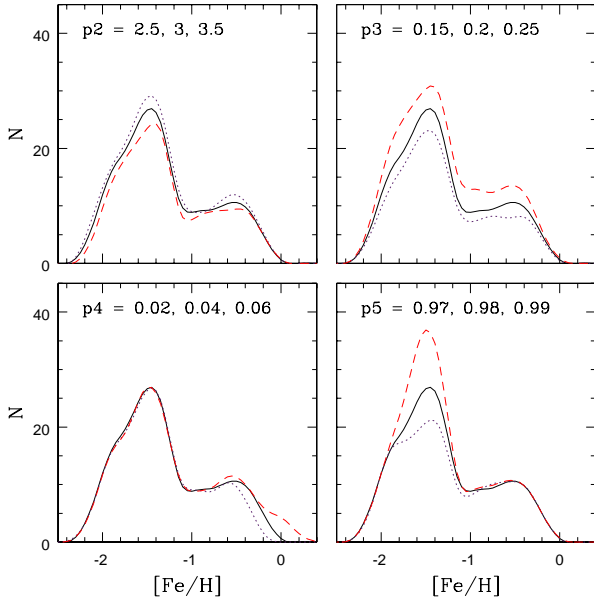


Figure 16. The effects of varying individual model parameters on the metallicity distribution. In each panel a single parameter is increased (*dotted line*) and decreased (*dashed line*) relative to the fiducial model (*solid line*). The parameter values are indicated inside the panels.

In this case, the metal-rich peak is severely depleted and remains only as an extended tail of a single-peaked, metal-poor distribution dominated by *case-2* clusters. These distributions are just some of the realizations of our model that were rejected due to their low values of \mathcal{L} . All of them have features that conflict with the observed metallicity distribution in the Galaxy.

4.4. Origin of the Metallicity Bimodality

The KS statistic measures the overall consistency of the model and observed metallicity distributions, but not specifically bimodality or multimodality within the distributions. In order to address the particular issue of modality, we employ two additional statistical tests, described in Appendix.

The Gaussian Mixture Modeling test indicates that the fiducial distribution is bimodal at a high level of significance (better than 0.1%). The peak metallicities of both modes and their widths are close to the observed values and agree with them within the errors. Both samples easily appear bimodal to the eye because the modes are well separated, with the dimensionless peak separation ratio $D > 3$ (see eq. A3). However, as we discuss in Appendix, the GMM test is sensitive to the assumption of Gaussian modes. It may indicate highly statistically significant split into two modes when the distribution is truly unimodal but skewed. For faster and more robust model selection we consider another test of multimodality.

The Dip test compares the cumulative input distribution with the best-fitting unimodal distribution. The maximum distance between the two corresponds to a dip in the differential distribution. The Dip test for the observed Galactic clusters indicates that the distribution is 90% likely to not be unimodal. When applied to our fiducial model, the Dip test implies it is 99% likely to not be unimodal. However, there is a caveat that the probability of the Dip test depends on the number of objects in the sample, similarly to KS test. The higher significance of the model result does not mean that the model

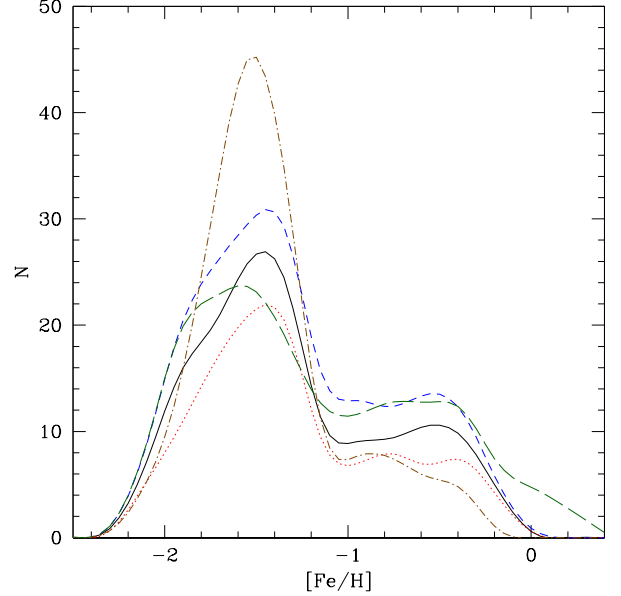


Figure 17. The effects of simultaneous variation of several model parameters. The fiducial model (*solid line*) is plotted alongside four distributions that illustrate other outcomes of our model. *Short-dashed* and *dotted lines* correspond to respectively lowering (to 0.15) and raising p_3 (to 0.3) away from its fiducial value (0.2). *Long-dashed line* corresponds to the model with $p_3 = 0.15$, $p_4 = 0$, $p_5 = 1$. *Dot-dashed line* corresponds to the model with $p_3 = 0.3$, $p_4 = 0.08$, $p_5 = 0.96$.

is actually more bimodal than the data, because we used all 11 random realizations of the model as a combined sample to evaluate the Dip test. While this is not a fair comparison to the data, it allows us to differentiate efficiently among alternative models.

We ran the Dip test for all models on the grid in a manner similar to the likelihood statistic. The most interesting result of the Dip statistic comes from one-dimensional slices of the parameter space. Considering only models with the normalized number of clusters in the range $140 < N < 160$, we binned the distributions according to the values of the four parameters and found the median and quartiles of P_{dip} in each bin. Figure 18 shows several trends. (i) Distributions with low formation rate p_2 are unlikely to be bimodal. The 75th percentile of P_{dip} increases systematically with p_2 in the range $2 < p_2 < 3$, but plateaus for $p_2 > 3$. (ii) The most bimodal distributions require p_3 to be small enough to allow for merger ratios 1:5 to trigger cluster formation. Between $p_3 = 0.2$ and $p_3 = 0.5$, the lower p_3 the better. However, mass ratios lower than 1:6 may dilute bimodality. (iii) The gas fraction threshold p_4 should be under 10% for ideal bimodality, to include mergers of massive galaxies. (iv) The fraction p_5 has to be close to 1, implying that *case-2* negatively affects bimodality. A conclusion from this plot is that bimodality appears in a significant number of model realizations, for a wide range of parameters. At the same time, a similarly large number of realizations are unimodal.

The metallicity distribution is bimodal if metal-rich clusters constitute a significant subset of all clusters. Thus, the fraction of red clusters, f_{red} , is a simple proxy for bimodality. Indeed, we find a strong correlation between f_{red} and P_{dip} . The red fraction follows similar, but weaker, trends with model parameters to those shown in Fig. 18. The median red fraction

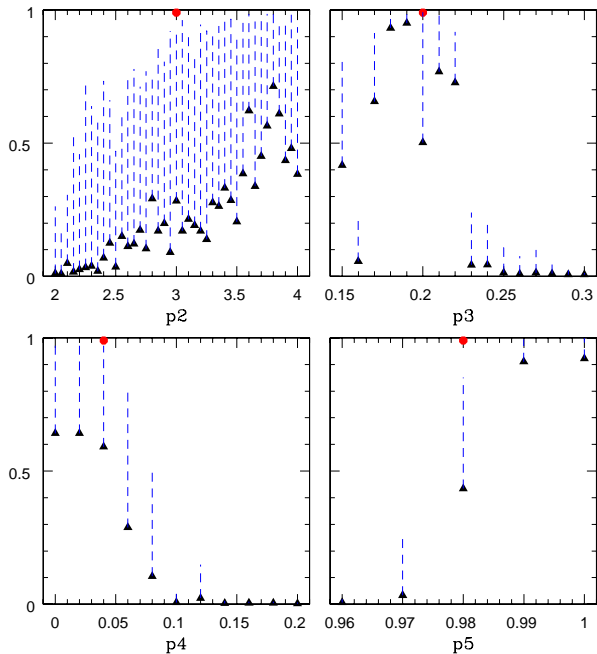


Figure 18. Median values of the Dip probability (*triangles*) among distributions with $140 < N < 160$, binned according to each parameter. Dashed lines extend to the 75% quartiles of P_{dip} . The fiducial model is shown by a red dot.

correlates most strongly with p_5 , increasing from $f_{\text{red}} = 16\%$ for $p_5 = 0.96$ to $f_{\text{red}} = 32\%$ for $p_5 = 1$. The red peak is significantly stronger without *case-2* clusters.

We note that the Dip test, unlike KS test, does not depend on comparing the model distribution to the Galactic sample. Therefore, the trends for bimodality derived from the Dip test should apply to other globular cluster systems. We anticipate that bimodality would likely arise if we applied our model with the parametric constraints stated above to any cosmological N -body simulation that follows the mass assembly history of a large galaxy. Further discussion of applying our model in different galactic environments follows in Section 7.

In order to investigate the underlying cause of bimodality, we examined various properties of merger events. A merger event is defined as any time in a halo's track when it meets the criteria for *case-1* formation. An important requirement here is the minimum mass of cold gas needed to produce a cluster that would survive dynamical disruption. Through equation (10), a cluster mass $M > 2 \times 10^5 M_{\odot}$ requires $M_g > 3 \times 10^8 M_{\odot}$. This constraint significantly reduces the number of eligible mergers. We considered the distributions of halo mass, lookback time, and metallicity (without additional dispersion) for all relevant merger events. We find that relatively few mergers happen in the space of high metallicity, high mass, and late time. Almost half of the mergers (44%) take place before $\tau = 12$ Gyr, and only 24% of the mergers happen in the last 10 Gyr. If we also counted the events that led to now-disrupted clusters, these numbers would spread even further to 53% and 17%, respectively. Nevertheless, the recent mergers stand out for two reasons: each such event creates more clusters, and these younger clusters have better chance of surviving the dynamical disruption than the older clusters. Since the number of clusters formed in each merger is positively correlated with the galaxy mass, the few stochastic super-massive mergers with high metallicity

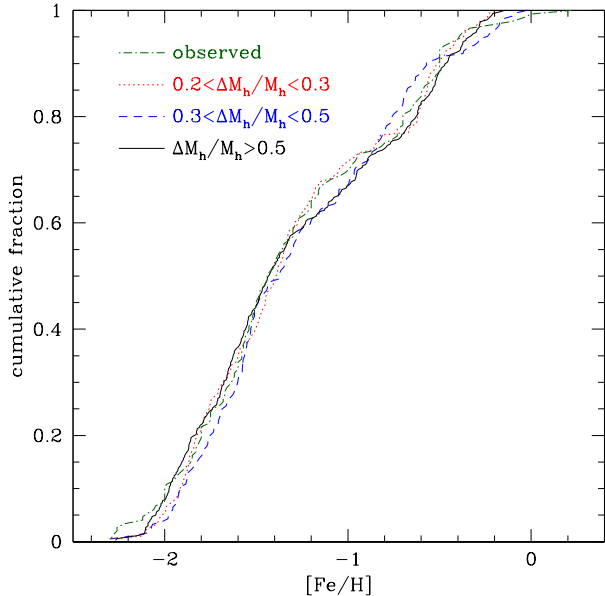


Figure 19. Cumulative metallicity distributions of the fiducial model clusters split by the range of merger mass ratios of their formation event: $0.2 < \Delta M_h/M_h < 0.3$ (*dots*), $0.3 < \Delta M_h/M_h < 0.5$ (*dashes*), and $\Delta M_h/M_h > 0.5$ (*solid line*). The similarity of all three distributions implies that metallicity bimodality is not caused by mergers with any particular range of mass ratios. The observed distribution is plotted in *dot-dashes* for comparison.

are likely to produce a significant number of clusters, which would separate the red peak from the blue peak.

We also considered that cluster bimodality may be linked to the mass ratios in the merger events. "Major" and "minor" mergers have been proposed to play different roles in galaxy formation, so it is conceivable that different types of star clusters may be formed depending on the merger ratio. In Figure 19 we plot cumulative metallicity distributions for clusters grouped according to the mass ratios in the cluster-forming merger event. Mergers with the closest masses, $\Delta M_h/M_h > 0.5$, contribute 48% of *case-1* clusters, while the lower two mass ranges each contribute equal portions of the rest. Running KS test on these distributions revealed that they formally represent statistically different populations. However, there is no clear-cut range of metallicities where one type of merging is exclusively producing all of the clusters, and the overall shapes of the distributions are similar. This uniformity suggests that bimodality is a natural consequence of hierarchical cluster formation regardless of the exact definition of a "major" merger.

Figure 20 shows how many models from the grid fall into particular ranges of the Dip probability and the ratio of *case-2* clusters to *case-1* clusters, N_2/N_1 . The models are restricted to have the normalized number of clusters $140 < N_1 + N_2 < 160$. The region with the highest density of models is in the lower-right corner of the plot, corresponding to high P_{dip} and low N_2/N_1 . Low values of P_{dip} are not significant since they cannot reject a unimodal distribution. Effectively, bimodality requires $N_2/N_1 \lesssim 0.5$. At the significance level of $P_{\text{dip}} = 90\%$, corresponding to the observed distribution, 38% of the grid models are bimodal if $N_2/N_1 < 0.3$. This fraction drops to only 15% for $0.3 < N_2/N_1 < 1$, and then further to 9% for $N_2/N_1 > 1$. These statistics confirms that bimodal populations appear only when the *case-2* channel is

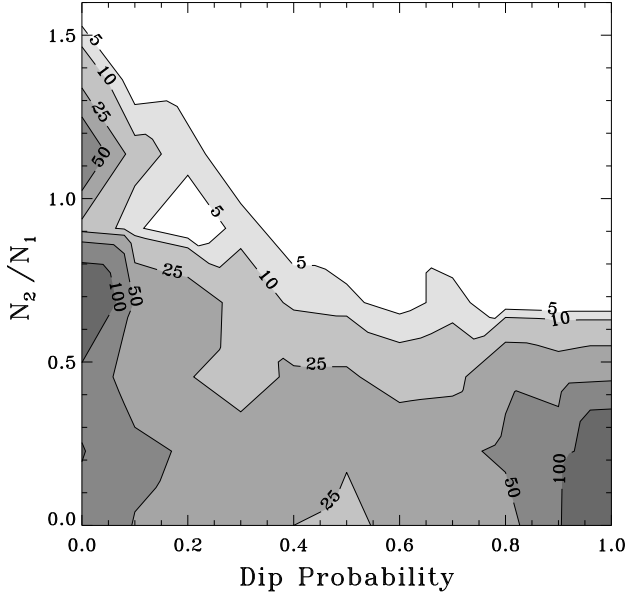


Figure 20. Number of models resulting in particular values of the Dip probability and the ratio of case-2 to case-1 clusters, for all realizations of the parameter grid with the normalized number of clusters $140 < N < 160$.

a secondary formation mechanism.

Another part of the explanation of bimodality of the surviving clusters is due to the dynamical evolution. Most of the disrupted clusters were old and blue. If we add these disrupted clusters to the metallicity histogram in the fiducial model, the blue peak rises by a factor of 2. The red peak remains virtually unaffected, since the more recently formed red clusters are less subjected to dynamical disruption. We ran the Dip test on all grid distributions, including both surviving and disrupted clusters. Among the models with the number of surviving clusters in the range $100 < N < 200$, few distributions have $P_{\text{dip}} > 50\%$ and none has $P_{\text{dip}} > 80\%$. This means virtually no bimodality. Indeed, the distributions appear almost entirely unimodal, with the peak in the blue end and nothing more than a tail in the red end. This leads to a prediction that late-type galaxies, which have more continuous cluster formation than early-type galaxies, may be less likely to exhibit bimodal cluster populations.

4.5. Alternative Formation Prescriptions

As alluded to in Section 2, some equations that we used in the prescriptions for the stellar mass and the cold gas fraction were based on only a few observed points. Currently there is limited observational or theoretical understanding of how these functions should behave at high redshift, which is the period of primary interest for our study. Below we consider some alternatives for these prescriptions.

The stellar fraction that we adopted from Woo et al. (2008) is well motivated by Milky Way dwarf galaxies at the present epoch, but the abundance-matching models such as the one by Conroy & Wechsler (2009) predict a steeper dependence on halo mass in the range $10^8 M_{\odot} < M_* < 10^{10} M_{\odot}$. Additionally, the redshift dependence of this relation is uncertain, and recent observational surveys (Borch et al. 2006; Bell et al. 2007; Dahlen et al. 2007) have advocated a slower evolution than $(1+z)^{-2}$ adopted in our model. To accommodate this uncertainty, we re-ran the entire parameter grid with equation

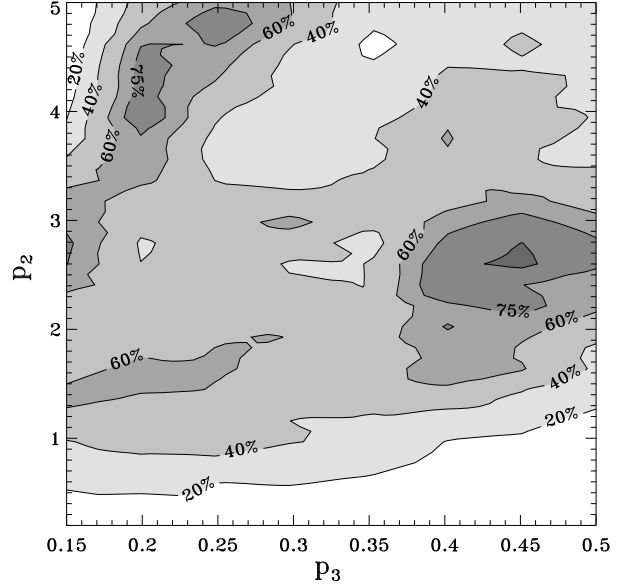


Figure 21. Same as Figure 13 but for the models with an alternative prescription for M_* as a function of M_h , given by equation (9).

(9) instead of equation (7). The corresponding contour plot is shown in Figure 21 and the best-fit metallicity distribution is shown in Figure 22. This best fit is capable of reproducing the observed metallicity ($P_{K,S,Z} = 49\%$) and mass distributions ($P_{K,S,M} = 9.5\%$), similar to our fiducial model. The acceptable range of the parameter space is narrower and shifted towards higher values of p_2 , as the steeper mass slope otherwise prevents low-mass halos from forming a sufficient number of clusters. Nevertheless, this alternative prescription still leads to a significant chance of a bimodal metallicity distribution.

Current observational constraints on the gas fraction at high redshift are even more uncertain. We adjusted the fit by altering the scale mass in equation (6). As alternatives to the fiducial model, we considered a power law of redshift, $M_s = M_{s,0}(1+z)^2$, and an inverse time dependence, $M_s = M_{s,0}(t/t_0)^{-1}$. Both of these relations resulted in lower gas fractions during the high-redshift epoch when most globular clusters should form. The gas fractions were too low for case-2 formation for any reasonable choice of p_5 . More importantly, the low gas masses did not allow even the most massive halos to form star clusters until intermediate redshifts. Therefore, none of these fits is a viable alternative to the fiducial model.

The same problems manifested if we took the simplistic approach of holding the gas fraction constant for all halo masses at all times. This idea was initially considered to see if we could generate simple results based only on halo merger histories without speculation on the baryonic physics. We quickly realized that this approach was not going to work. Setting f_g too low effectively prevents cluster formation at high redshift, when blue globular clusters are expected to form, as most halos cannot build up sufficient mass to overcome the minimum mass required to form a single massive star cluster (discussed in Section 2.2). A constant gas fraction that is too high, on the other hand, presents obvious unphysical predictions at low redshift, and in particular would drastically over-predict the number of young clusters, forcing us to arbitrarily truncate

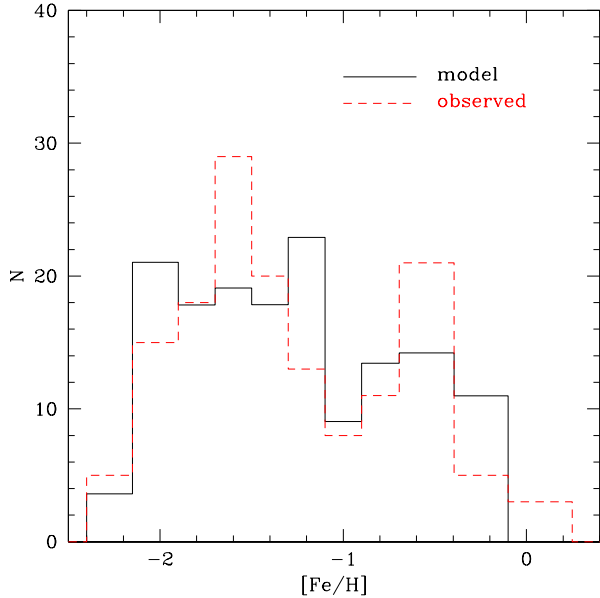


Figure 22. Metallicity distribution at $z=0$ in the best-fit model with an alternative prescription for M_* as a function of M_h , given by equation (9) (solid histogram), compared to the observed distribution of Galactic globular clusters (dashed histogram).

their formation.

We also considered an alternative parametrization of the gas fraction, suggested by Stewart et al. (2009). They took the same observational constraints as us, but fitted them as

$$\frac{M_g}{M_*} = 0.04 \left(\frac{M_*}{4.5 \times 10^{11} M_\odot} \right)^{-0.59(1+z)^{0.45}}. \quad (27)$$

This formula predicts so much cold gas at high redshift that many low-mass halos would be able to form clusters via *case-2* channel for any $p_5 < 1$. If we completely disable *case-2* formation and use the above prescription for the gas mass, we find many model realizations consistent with the observed metallicity distribution. This prescription differs from our fiducial choice in that it produces considerably more young clusters and achieves less clear metallicity bimodality. The maximum value of the likelihood function attainable with this prescription is approximately half of the value for the fiducial prescription. Nevertheless, it could still produce acceptable globular cluster results.

In addition to changing the formulation of the fits, we investigated the effect of adding a random Gaussian dispersion with standard deviation σ_{fits} to the right hand sides of equations (3), (5), and (7) to reflect their intrinsic scatter as well as observational uncertainty. Different random values for the three scatters are generated for each halo at each timestep, but we always force the condition (8) on the total baryon content. For simplicity, we used the same magnitude of σ_{fits} for the scatter added to all three equations simultaneously. We re-ran the parameter search grid using $\sigma_{\text{fits}} = 0.1, 0.2,$ and 0.3 dex. For each value of σ_{fits} , we were still able to find models with high values of $P_{K,S,Z}$ and overall likelihood statistic, although these values decline with the increasing amount of scatter. The metallicity probability varies from 49% to 16% to 6%, for $\sigma_{\text{fits}} = 0.1, 0.2, 0.3$ dex respectively.

As an alternative to scatter in the cutoff mass (eq. 3) with

a fixed functional form for the gas fraction (eq. 2), we tried adding scatter to equation (2) while keeping fixed equation (3). Adding scatter to f_{in} allows the gas fraction to exceed the threshold p_5 much more easily and produce too many *case-2* clusters. To avoid unphysical results, we analyze only results for *case-1* formation. In this case we find the best-fit models with $P_{K,S,Z} = 47\%, 13\%,$ and 5% , for $\sigma_{\text{fits}} = 0.1, 0.2, 0.3$ dex respectively. These models are still consistent with the observed Galactic distribution.

The addition of scatter as described above has two systematic effects on any individual realization of the metallicity distribution: the high metallicity tail is extended even further and the height of the blue peak is damped relative to the case of no scatter. The former effect is due to the possibility of drawing higher values of M_* and hence higher $[\text{Fe}/\text{H}]$. The latter effect arises from the enforcement of equation (8), which prevents gas-rich halos at high-redshift from gaining any extra gas from the positive scatter in equation (5); on the other hand, negative scatter can prevent some of these halos from being eligible for *case-2* formation. Accordingly, the best distributions with higher values of σ_{fits} were found for models with low values of p_5 . We note that the Dip probability in most realizations is not strongly affected by the new scatter, implying that the actual smearing of the peaks is not significant and bimodality is preserved.

4.6. Alternative Dynamical Disruption

In Section 3 we noted that the expression for the evaporation rate (eq. [23]) contains some inherent parameters. Here we explore alternative disruption models with different values of ξ_e and δ within the fiducial formation prescription.

The effect of decreasing ξ_e is simply to reduce the number of clusters that are completely disrupted by $z=0$. In the fiducial model with $\xi_e = 0.033$, about 60% of the original sample is disrupted. (Note that this implies that roughly $5 \times 10^7 M_\odot$ worth of stars in the Galactic stellar halo could be remnants of the disrupted clusters.) With the factor of $\xi_e = 0.02$, only $\sim 30\%$ are disrupted. With the factor of $\xi_e = 0.01$, almost all clusters survive.

The effect of decreasing δ and δ_0 is to shift the peak of the mass function to a lower mass.

We repeated the grid parameter search for the best metallicity distribution for two alternative prescriptions, one with $\xi_e = 0.02$, $\delta = \delta_0 = 1/3$, and the other with $\xi_e = 0.033$, $\delta = \delta_0 = 1/9$. We found that in both cases our model could produce an observationally-consistent metallicity distribution. However, lowering either ξ_e or δ significantly alters the mass function away from the data, by allowing too many low-mass clusters to survive. Raising ξ_e and δ may improve the mass function, but steers away from recent constraints on the two parameters (Baumgardt & Makino 2003; Gieles & Baumgardt 2008). Therefore, we ultimately conclude that our fiducial prescription ($\xi_e = 0.033$, $\delta = \delta_0 = 1/3$) works best.

For illustration, we list below the properties of the best models in the two alternative prescriptions. For $\xi_e = 0.02$, $\delta = \delta_0 = 1/3$, we find a peak model that has a metallicity distribution with $P_{K,S,Z} = 69\%$ and mass distribution with $P_{K,S,M} = 0.02\%$. The parameters of this model are $p_2 = 4.4$, $p_3 = 1.4$, $p_4 = 0$, $p_5 = 0.99$.

For $\xi_e = 0.033$, $\delta = \delta_0 = 1/9$, we find a peak model that has a metallicity distribution with $P_{K,S,Z} = 19\%$ and mass distribution with $P_{K,S,M} = 12\%$. The parameters of this model are $p_2 = 4$, $p_3 = 1.4$, $p_4 = 0$, $p_5 = 0.97$. Its metallicity distribution is shown in Figure 23. The overabundance of metal-poor

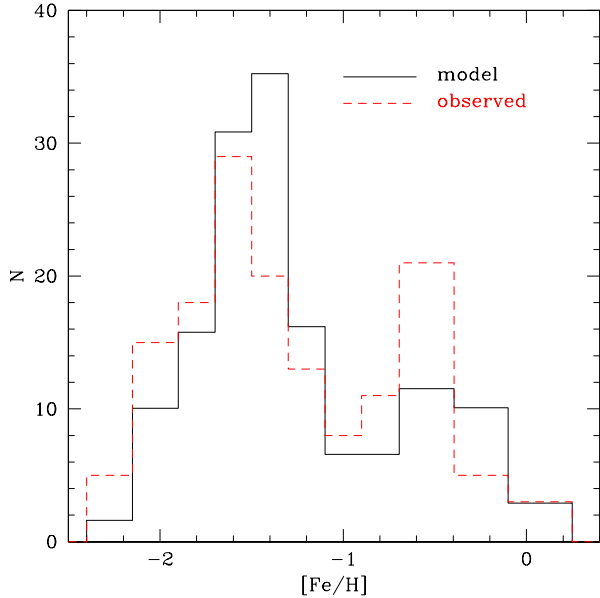


Figure 23. Metallicity distribution at $z = 0$ in the best-fit model with an alternative dynamical disruption prescription, $\delta = \delta_0 = 1/9$ (solid histogram), compared to the observed distribution of Galactic globular clusters (dashed histogram).

clusters is clear.

The latter alternative prescription ($\delta = 1/9$) predicts the disruption time to scale with cluster mass in a manner nearly identical to Gieles & Baumgardt (2008), if we take that all model clusters have a mean galactocentric frequency $\omega = (2.4 \times 10^7 \text{ yr})^{-1}$. Based on the orbit calculations discussed in the next section, we find a similar median value of ω for the sample of model clusters in the fiducial model. We also find no correlation between ω and cluster mass, which confirms our assertion in Section 3 that in such a model the disruption time of the average cluster would scale with mass as $\nu_{\text{ev}}^{-1} \propto M^{2/3}$.

5. SPATIAL DISTRIBUTION

Using the same N -body simulation as in this paper, Prieto & Gnedin (2008) investigated the present spatial distribution of model clusters that formed in high-redshift (metal-poor) galactic systems. They calculated the orbits of clusters from the time when their host galaxies accreted onto the main galaxy and identified three distinct populations. *Disk clusters* formed in the most massive halo that eventually hosts the present Galactic disk. These clusters, found within the inner 10 kpc, are scattered into eccentric orbits by the perturbations from accreted galactic satellites. *Inner halo clusters*, found between 10 and 60 kpc, came from the now-disrupted satellite galaxies. Their orbits are inclined with respect to the Galactic disk and are fairly isotropic. *Outer halo clusters*, beyond 60 kpc from the center, are either still associated with the surviving satellite galaxies, or were scattered away from their hosts during close encounters with other satellites and consequently appear isolated.

The azimuthally-averaged space density of metal-poor globular clusters is consistent with a power law, $n(r) \propto r^{-\gamma}$, with the slope $\gamma \approx 2.7$. Since all of the distant clusters originate in progenitor galaxies and share similar orbits with their

hosts, the distribution of the clusters is almost identical to that of the surviving satellite halos. This power law is similar to the observed slope of the metal-poor globular clusters in the Galaxy. However, the model clusters have a more extended spatial distribution (larger median distance) than observed. In the model it is largely determined by the orbits of the progenitor galaxies and the epoch of formation. Moore et al. (2006) showed that the early-forming halos are more spatially concentrated and in order to match the Galactic distribution, globular clusters would need to form at $z \sim 12$. However, such an early formation may be inconsistent with the requirement of high mass and density of the parent molecular clouds.

In this work, we have retraced some of these steps to attempt to reproduce the spatial distribution of the whole Galactic globular cluster system.

The clusters that formed in the disk of the main halo are assigned radial positions according to the exponential profile, $dN/dR \propto R e^{-R/R_d}$, with the observed scale length of the Galactic disk, $R_d = 3$ kpc. The azimuthal angles are assigned randomly. The vertical position in the disk is also assigned randomly, with the scale-height of one fifth of the scale-length. The clusters are limited to the radial range $0.6 < R < 10$ kpc, where the observed disk globular clusters are located. The distances are also given a random Gaussian scatter of 10% to replicate observational distance uncertainties.

Clusters that formed in satellite halos that survived until $z = 0$ are assigned the present position of the host, with a small displacement analogous to the distribution in the main disk. Clusters that formed in subhalos that did not survive until $z = 0$ are initially assigned the last known position and velocity of the host in the simulation, with the same displacement as above. We then follow the orbits of these stray clusters until $z = 0$ using a leap-frog integration scheme with fixed time step.

The orbit integration follows Prieto & Gnedin (2008). The main halo and the satellite halos contribute their NFW potentials, while the disks within the halos contribute the Miyamoto-Nagai potentials with the total mass of gas and stars computed from equations (5) and (7). The total gravitational potential is computed by linearly interpolating the masses of halos and subhalos between the simulation snapshots. Positions of subhalos at each timestep are computed with cubic splines between the snapshots. We also include the acceleration on the clusters that results from the use of the splines, as described in Prieto & Gnedin (2008). Cosmological dark energy contributes an additional component to the acceleration in physical coordinates: $\mathbf{a}_\Lambda = \Omega_\Lambda H_0^2 \mathbf{r}$.

Just as in the previous study, we find a more extended spatial distribution of the globular cluster system than that observed in the Galaxy. Clusters that formed in surviving satellites (about 24% of the sample in the fiducial model) are the most distant from the center, as forced by the location of the satellites. The orbit integration for the clusters formed in disrupted satellites (about 52% of the sample) shows that these clusters also do not migrate in r far from the last known position of their host. Such coupling to the dark matter halos is the main reason for the overextended cluster system.

Clusters that formed in the disk of the main halo (the remaining 24% of the sample) most closely resemble the spatial properties of the Galactic clusters. They are confined to the inner 10 kpc and would be referred to as the bulge or disk clusters. However, this group should contain more than 50% of the sample to be consistent with observations. Recent paper

by Griffen et al. (2010) similarly investigated the formation of red clusters by major mergers in the Aquarius simulation and concluded that such clusters must have formed in the central disk.

Note that our orbit calculations, as well as those by Griffen et al. (2010), use the gravitational potential derived in collisionless cosmological simulations. Stars and cold gas would deepen the gravitational potential in the inner regions of the main halo and bring the satellites closer to the center. Dense stellar nuclei of the satellites should also survive against tidal disruption longer than pure dark matter halos. Hydrodynamic simulations of Naab et al. (2009) show that the combined effect of baryons may be to deposit half of stellar remnants of the disrupted satellites, including their globular clusters, within 10 kpc of the center. This would effectively reconcile the predicted cluster distribution with the Galactic sample, since over 50% of our clusters formed in disrupted satellites. More detailed hydrodynamic simulations of galaxy formation are needed to verify either hypothesis.

An observational test of the cluster orbits would be possible when proper motions are measured for a large fraction of the Galactic clusters. Such measurements could be achieved with the planned SIM-Lite space observatory.

6. GLOBULAR CLUSTER COLORS

We attempted another direct comparison of the model predictions with the observed sample, by constructing single stellar population models using Bruzual & Charlot (2003) code GALAXEV. As input for GALAXEV, we used the age and metallicity for each globular cluster created with the fiducial model.

The distribution of the model $B-V$ color was considerably less bimodal than the metallicity distribution discussed in previous sections. The main cause of the smearing of the two peaks appears to be the younger age of metal-rich clusters predicted by the model. The metal-poor clusters constitute a clearly defined peak at $B-V = 0.67$, which corresponds well to the blue peak of the Galactic sample. But the metal-rich clusters, which are expected to make up the red peak, have a mean $B-V$ color of 0.77, while the observed red mean is close to 0.85. The standard deviation of the red model clusters is 0.08, implying that the result is consistent within one sigma of the observed, but the bimodality of the distribution is not evident to the eye.

To test the hypothesis that the smearing of the color peaks compared was due to the relative age of the populations, we ran the population synthesis models again, this time using a constant age of 12.1 Gyr for all clusters. The resulting distribution indeed appeared to constitute two peaks, with a blue peak at a mean of $B-V = 0.67$ and a red peak at $B-V = 0.84$, with a clearly defined gap between them. It should be noted that a known discrepancy exists between the $B-V$ colors predicted by all major population synthesis codes and those of observed globular clusters (Conroy & Gunn 2010). All models predict colors that are too blue at high metallicity, which would directly play into smearing bimodality in our result.

In addition to the colors, we examined the cluster luminosities (absolute V -band magnitudes) calculated by GALAXEV. These allow a more direct comparison with the observations than the mass function presented in Section 3, for which we were required to assume a constant mass-to-light ratio for all observed clusters. This constant M/L_V ratio has been a traditional approach, but has come under recent scrutiny by Krujssens (2008) who argued that M/L_V may vary as a func-

tion of cluster mass. However, the distribution of V -band magnitudes for our fiducial model has a KS probability of 4.3%, which is not a significant departure from the 7.4% for the mass function. When we tried the same exercise as above by setting the ages of all model clusters to 12.1 Gyr, the KS probability jumped to 25%. This improvement likely happened because we converted the magnitudes of observed clusters into masses using $M/L_V = 3$, while GALAXEV typically predicted $M/L_V < 3$ for the 12.1 Gyr isochrones. This brought the mean luminosity of model clusters closer to the observed value than the average mass of model clusters was to its observed counterpart.

Even though these population synthesis results are interesting, we believe that the mass and metallicity distributions presented in previous sections are more reliable. Population synthesis modeling adds an extra layer of empirical uncertainty to our results, as the specific nature of horizontal-branch evolution remains an issue that has not been completely resolved.

7. SUMMARY AND IMPLICATIONS FOR GALAXY FORMATION MODELS

We have presented a model for the origin of the metallicity distribution of globular clusters. In our scenario, bimodality results from the combination of the history of galaxy assembly (rate of mergers) and the amount of cold gas in protogalactic systems. Early mergers are frequent but involve relatively low-mass protogalaxies, which produce preferentially blue clusters. Late mergers are infrequent but typically involve more massive galaxies. As the number of clusters formed in each merger increases with the progenitor mass, just a few late massive mergers can produce a significant number of red clusters. The concurrent growth of the average metallicity of galaxies between the late mergers leads to an apparent ‘‘gap’’ between the red and blue clusters.

The peak metallicities of the red and blue populations are remarkably robust to variations of the model parameters. The peaks encode the mass-metallicity relation in galaxies and do not depend strongly on the rate or timing of cluster formation. The exact definition of a major merger is also not important for our result, as long as the merger mass ratio is at least 1:5.

Our conclusions on the origin of metallicity bimodality are not significantly affected by the large uncertainties in our knowledge of the stellar mass and cold gas mass in high-redshift galaxies. We considered alternative prescriptions for the stellar fraction, gas-to-stars ratio, and even dynamical disruption, but in all cases found a metallicity distribution consistent with the observations. Such robustness indicates that most external factors are not as important as the internal mass-metallicity relation in host galaxies.

We find that dynamical disruption over the cosmic history naturally converts an initial power-law cluster mass function into an observed log-normal distribution. A continuous formation of clusters in the first several Gyr help to replenish the depleted low-mass end. Dynamical disruption also helps establish metallicity bimodality by preferentially depleting old clusters in the metal-poor peak.

Our prescription links cluster metallicity to the average galaxy metallicity in a one-to-one relation, albeit with random scatter. Since the average galaxy metallicity grows monotonically with time, the cluster metallicity also grows with time. Our model thus encodes an age-metallicity relation, in the sense that metal-rich clusters are somewhat younger than their metal-poor counterparts. Observations of the Galactic globular clusters indicate an age spread that ranges from 1 Gyr for

the inner blue clusters to 2 Gyr for the inner red clusters to 6 Gyr for the outer clusters, which is generally consistent with the predicted spread. However, the model may be marginally inconsistent with the observation that some of the metal-rich clusters appear as old as the metal-poor ones. Note that our model is still simplistic and does not include metallicity gradients within protogalaxies, which may dilute the predicted age-metallicity relation.

Our model demonstrates that star cluster formation during gas-rich mergers of protogalactic systems is a single mechanism that successfully reproduces many observed properties of the Galactic globular clusters. It may avoid the need for two separate formation mechanisms for the red and blue clusters invoked in the model of Beasley et al. (2002). Their model relied on constant cluster formation efficiency relative to the field stars, but required different efficiencies for the two modes. While the red clusters in their models continued forming through galaxy mergers, the blue clusters needed to be arbitrarily shut off at $z = 5$. This was the main cause of the bimodal metallicity distribution in their model, as the blue clusters did not have much overlap with the red clusters that formed in major mergers involving metal-enriched gas considerably after $z = 5$. The Beasley et al. (2002) model also neglected the effects of the dynamical evolution that shaped the present cluster distribution. In contrast, in our model some old blue clusters are disrupted and some are unable to form at recent times because the protogalaxies are gas-poor. Another difference is that in our model major mergers contribute both red and blue clusters, while in Beasley et al. they contribute only red clusters. We also find that globular clusters form significantly earlier than the bulk of field stars and therefore the two cannot be linked by a constant formation efficiency at all times (see Fig. 10).

We have compared the metallicity distribution of globular clusters to the mass-weighted metallicity distributions of other stellar populations as predicted by our scaling relations given in Section 2. We find that galaxy field stars overall have a single-peaked distribution with a mean of $[\text{Fe}/\text{H}] \approx 0$, a metal poor tail, and no stars with $[\text{Fe}/\text{H}] > 0.4$. This is consistent with our current understanding of the metallicity of stars in the Galactic disk. The stars in surviving satellites, which correspond to Milky Way dwarf galaxies, also appear to have a single-peaked distribution with a mean metallicity $[\text{Fe}/\text{H}] \approx -1$. Only the globular cluster system display a bimodal metallicity distribution.

We derived some simple scaling relations for the overall efficiency of globular cluster formation. We adopted the cluster formation rate in gas-rich, high-redshift merger events (eq. 10) that scales with the host system mass as $M_{GC} \sim 10^{-4} M_g / f_b \sim 10^{-4} M_h$. We have later learned of a similar empirical relation for all types of massive galaxies, derived independently by Spitler & Forbes (2009) and Georgiev et al. (2010). The outcome of the model is a prediction that the fraction of galaxy stellar mass locked in star clusters, M_{GC}/M_* , is of the order 10–20% at $z > 3$ and then declines steadily with time to about 0.1% at present. The specific frequency parameter follows a similar decline with time and reaches $N/(M_*/10^9 M_\odot) \sim 1$ at the present. These efficiencies are in agreement with the compilations of McLaughlin (1999),

Rhode et al. (2005), and Peng et al. (2008). We also find that the globular cluster system overall is significantly more metal-poor than the galactic spheroid, which is populated by stars from the disrupted satellites.

Our scenario can be applied to other galactic environments, such as those of elliptical galaxies which contain much larger samples of globular clusters. For example, Peng et al. (2008) showed that the fraction of red clusters increases from 10% to 50% with increasing luminosity of elliptical galaxies in the Virgo cluster. In our model, globular cluster formation is entirely merger-driven. We showed that the Galactic sample may have arisen from early super-gas-rich low-mass mergers and later metal-rich high-mass mergers. Compared to the Galaxy, giant ellipticals are expected to experience more high-mass mergers which would contribute more prominently to the globular cluster system. As Figure 7 shows, such mergers would produce comparable numbers of red and blue clusters simultaneously. Thus the fraction of red clusters should increase with galaxy mass, reaching $\sim 50\%$ for giant ellipticals. This trend, observed by Peng et al. (2008), may be a natural outcome of the hierarchical formation.

At the other end of the galactic spectrum, dwarf galaxies likely lacked metal-rich mergers and produced only metal-poor blue clusters. In particular, dE and dSph type dwarfs which are now deprived of cold gas are not expected to contain any young and metal-rich clusters. Some dIrr galaxies, such as the LMC, still possess considerable amounts of cold gas and may produce younger clusters, although they are still likely to have subsolar metallicity. The variety of globular cluster ages observed in the LMC indicates that it may have had bursts of star formation throughout its cosmic evolution.

Our study places interesting constraints on galaxy formation models. Within the framework of our model, acceptable mass and metallicity distributions result only from a certain range of the parameters. In particular, the minimum ratio of masses of merging protogalaxies strongly correlates with the cluster formation rate. If the clusters form very efficiently only a few massive mergers are needed; if the clusters form inefficiently many mergers are needed, which requires a lower merger threshold. However, mass ratios of less than 0.2 are disfavored in the model (see Fig. 13). Formation of massive clusters in very gas-rich systems without detected mergers (our case-2 scenario) improves the final mass function but is not required for reproducing the metallicity distribution. Thus, globular cluster formation solely in major mergers is consistent with the available observations. Finally, our results rest on the derived prescription for the cold gas fraction as a function of halo mass and cosmic time. This prescription (Fig. 1) can be tested by future observations of high-redshift galaxies with JWST and by detailed hydrodynamic simulations.

We would like to thank Kerby Shedden for a discussion of statistical methods regarding bimodality, Steve Zepf for a copy of the original KMM code, Karl Gebhardt for a discussion of the Dip test, Martin Maechler for an updated probability table of the Dip test, Evan Kirby for a discussion of metallicities of the ultrafaint dwarfs, and Eric Bell, Nick Gnedin, Andrey Kravtsov, and Lee Spitler for comments on the manuscript.

APPENDIX

QUANTIFYING BIMODALITY

Quantifying whether a distribution is better described by one or two modes is still an unsolved problem in statistics. While there are algorithms that split the input distribution into two modes or assign probabilities that a given data point belongs to either of the two modes, there is no proper statistic that evaluates whether such a split is preferred to a unimodal distribution. In this Appendix, we describe a popular KMM algorithm and our improvement of it, as well as an independent test of bimodality based on the Dip statistic.

GMM – A better version of KMM

Ashman et al. (1994) popularized a mixture modeling code KMM for detecting bimodality in astronomical applications. This code has been widely used for globular cluster studies and can be considered a standard method in the field. The KMM algorithm assumes that an input sample is described by a sum of two Gaussian modes and calculates the likelihood of a given data point belonging to either of the two modes. It also calculates the likelihood ratio test (LRT) as an estimate of the improvement in going from one Gaussian to two Gaussian distributions. However, the LRT obeys a standard χ^2 statistic only when the two modes have the same width (variance), which may not be satisfied by real datasets. Even though the probability of the LRT can be estimated using bootstrap in principle, in practice the use of the KMM code has been limited to common width modes (the so-called “homoscedastic” case). Brodie & Strader (2006) and Waters et al. (2009) provide further discussion of KMM.

The KMM method belongs to a general class of algorithms of Gaussian mixture modeling (GMM). GMM methods maximize the likelihood of the data set given all the fitted parameters, using the expectation-maximization (EM) algorithm (e.g., Press et al. 2007). A major simplification, which allows one to derive explicit equations for the maximum likelihood (ML) estimate of the parameters, is that each mode is described by a Gaussian distribution.

For simplicity, and as appropriate for the metallicity distribution, we consider a univariate input data set. However, the algorithm is fully scalable to multivariate distributions. The likelihood function of a univariate sample x_n is

$$\mathcal{L}_K = \prod_n \left(\sum_{k=1}^K p_k N(x_n | \mu_k, \sigma_k) \right), \quad (\text{A1})$$

where

$$N(x | \mu, \sigma) = \frac{1}{(2\pi\sigma^2)^{1/2}} \exp \left[-\frac{(x-\mu)^2}{2\sigma^2} \right] \quad (\text{A2})$$

is the Gaussian density. The modal fractions are normalized as $\sum_k p_k = 1$. A unimodal distribution ($K = 1$) has two independent parameters (μ and σ), whereas a bimodal distribution has five parameters ($p_1, \mu_1, \sigma_1, \mu_2, \sigma_2$), since $p_2 = 1 - p_1$.

The power of the GMM method lies in its ability to determine the ML values of the parameters (p_k, μ_k, σ_k). The disadvantage is that the method will always split the data set into the specified number of modes, K . In order to detect bimodality it is extremely important to be able to judge whether the bimodal fit is an improvement over the unimodal fit. For this purpose the KMM code uses the LRT test, which appears to be an approximation derived by Wolfe (1971) for the homoscedastic case ($\sigma_1 = \sigma_2$). Define the ratio of the maximum likelihoods as $\lambda \equiv \mathcal{L}_{1,\max} / \mathcal{L}_{2,\max}$. According to numerical Monte Carlo studies of Wolfe (1971), the statistic $-2 \ln \lambda$ approximately obeys the χ^2 distribution with a number of degrees of freedom equal to “twice the difference between the number of parameters of the two models under comparison, not including the mixing proportions” (McLachlan 1987). This is the χ^2_2 distribution in our case. However, the statistic does not apply in the heteroscedastic case $\sigma_1 \neq \sigma_2$ (it would have been χ^2_4). Note that this unusual number of degrees of freedom was found as an empirical approximation. Unfortunately, no exact estimation exists for the goodness of modal split.

Several variations of the method have been suggested in the literature. McLachlan (1987) proposed a *parametric bootstrap* to test for the number of components. In this method, a test sample is drawn randomly from a unimodal Gaussian distribution with the parameters $\{\mu, \sigma\}$ best-fitting the input sample. The number of objects in the test sample is taken the same as in the input sample. The bimodal split is calculated for this test sample using the EM algorithm and the likelihood ratio λ_{boot} is saved. Repeating the bootstrap a large number of times, we obtain the probability of randomly drawing the ratio as large as that observed in the input sample, λ_{obs} . If the probability is below a few percent, we reject the null hypothesis that the input sample belongs to a unimodal Gaussian.

However, the parametric bootstrap is not a perfect solution. In the limit of a large number of objects in the input sample, the likelihood function is very sensitive to outliers far from the center of the distribution. Simple measurements errors in the wings of the Gaussian function may cause a unimodal distribution to be rejected, even if it is correct. In other words, GMM is more a test of Gaussianity than of unimodality (see Muthén 2003; Bauer 2007, for more discussion).

Lo et al. (2001) proposed a modified LRT method to test for the true number of components of a Gaussian mixture. The modified statistic must be evaluated numerically, but still does not address the problem with Gaussian wings. Subsequently, Lo (2008) suggested to use the standard LRT with the parametric bootstrap to test for heteroscedastic split, and also suggested restricting the ratio of the standard deviations of the two modes to be not less than 0.25, to avoid numerical artifacts. Such a method was recently implemented in globular cluster studies by Waters et al. (2009).

The sensitivity of LRT to the assumption of Gaussian distribution calls for additional, independent tests of bimodality. A useful

and intuitive statistic is the separation of the means relative to their widths:

$$D \equiv \frac{|\mu_1 - \mu_2|}{[(\sigma_1^2 + \sigma_2^2)/2]^{1/2}}. \quad (\text{A3})$$

We use the factor $\sqrt{2}$ for consistency with the definition in Ashman et al. (1994), who noted that $D > 2$ is required for a clean separation between the modes. If the GMM method detects two modes but they are not separated enough ($D < 2$), then such a split is not meaningful. The power of GMM in this case is counterproductive. A histogram of such a distribution would show no more than two little bumps, which would not be recognized as distinct populations.

Another simple statistic is the kurtosis of the input distribution. A positive kurtosis corresponds to a sharply peaked distribution, such as the Eiffel Tower. A negative kurtosis corresponds to a flattened distribution, such as a top hat. A sum of two populations, not necessarily Gaussians, is broader than one population and therefore has a significantly negative kurtosis. However, $kurt < 0$ is a necessary but not sufficient condition of bimodality. A broad unimodal distribution, such as an actual top hat, also has negative kurtosis. Therefore, $kurt < 0$ is only useful as an additional check to support the results of LRT and the D -value.

In order to provide a more robust measure of the modal split, we have revised and implemented the GMM algorithm independently of the KMM code. We begin with a single run of the EM algorithm to calculate the means and standard deviations assuming a heteroscedastic bimodal distribution. Then we repeat the estimation assuming a unimodal Gaussian case. We take the ratio of the likelihoods λ , the separation D , and the kurtosis as the three statistics of interest. We then estimate the error distribution for the modal parameters using non-parametric bootstrap (drawing from the input sample with repetitions) of 100 realizations. We also run the parametric bootstrap to assess the confidence level at which a unimodal distribution can be rejected based on each of the three statistics. Its practical application for an input sample of more than 100 objects is limited to about 1000 bootstrap realizations, limiting the confidence level to $\sim 10^{-3}$. A sufficiently low probability of each statistic means a unimodal distribution can be rejected in favor of a bimodal distribution. The code also calculates the probability of each data point belonging to either mode.

A sum of two Gaussians with the same variance can sometimes be preferred to the case of different variances, because of the one fewer degree of freedom. The choice between the homoscedastic and heteroscedastic cases can be similarly made using LRT, but we feel that it is less important than choosing between a bimodal and unimodal distributions. For comparison with the KMM code, we calculate the homoscedastic split and its approximate probability using the χ^2_2 statistic. We also calculate an alternative split into two Gaussian modes with the same mean but different variance. This is a more extended distribution than a single Gaussian, which may be a better fit for a unimodal but non-Gaussian sample.

The steps of our algorithm are summarized below:

1. Calculate $\{\mu, \sigma\}$ and $\{p_1, \mu_1, \sigma_1, \mu_2, \sigma_2\}$ using a single EM run.
2. Form three statistics: λ , D , and $kurt$.
3. Run non-parametric bootstrap to estimate the errors: $\Delta\mu_k$, $\Delta\sigma_k$, Δp_1 , and ΔD .
4. Run parametric bootstrap to estimate the probability of a unimodal distribution, according to λ , D , and $kurt$.

As a first test of the algorithm, we verified that it reproduces exactly the test output of the KMM code, given the test input provided with the code.

We also made two random realizations of a unimodal Gaussian distribution, $N(0, 1)$, with 150 objects and 1500 objects, respectively. The smaller sample has the mean and standard deviation of $\mu = -0.088$ and $\sigma = 0.987$, within the intended target given the sample size. Indeed, a non-parametric bootstrap gives $\Delta\mu = 0.084$, $\Delta\sigma = 0.063$. The kurtosis of the input sample is $kurt = 0.104$. A heteroscedastic split gives two peaks, by construction, with $\mu_1 = -0.483$, $\sigma_1 = 1.206$ and $\mu_2 = -0.032$, $\sigma_2 = 0.938$. However, the split is not statistically significant. The likelihood is improved only by $-2 \ln \lambda = 0.26$ relative to the unimodal case, which gives the probability better than 99% that the input sample is unimodal. The parametric bootstrap gives a similar probability of 96%. The separation of the peaks also leads to the same conclusion: $D = 0.42 \pm 1.46$. The parametric bootstrap probability of drawing such value of D randomly from a unimodal distribution is 87%. The probability of drawing the measured kurtosis is 74%. Thus, all three statistics show correctly that the input distribution is not bimodal. The larger test sample has smaller parameter errors, as expected, but similar significance levels from the parametric bootstrap.

We then apply the GMM algorithm to the sample of observed metallicities of the Galactic globular clusters. A unimodal fit gives $\mu = -1.298 \pm 0.049$ and $\sigma = 0.562 \pm 0.028$, where the errors are calculated with the non-parametric bootstrap. A heteroscedastic split gives $\mu_1 = -1.608 \pm 0.064$, $\sigma_1 = 0.317 \pm 0.051$ and $\mu_2 = -0.583 \pm 0.074$, $\sigma_2 = 0.281 \pm 0.075$. Of the total number of 148 clusters, 103 (or 70%) are in the metal-poor group and 45 (or 30%) are in the metal-rich group. A homoscedastic split gives $\mu_1 = -1.620 \pm 0.037$, $\mu_2 = -0.608 \pm 0.055$, and $\sigma_1 = \sigma_2 = 0.303 \pm 0.026$. In this case, there are 101 metal-poor clusters and 47 metal-rich clusters. In either case, the likelihood improvement in the 1000 parametric bootstrap realizations is never as high as observed, $-2 \ln \lambda = 27.5$. That is, a unimodal distribution is rejected at a confidence level better than 0.1%. The separation of the peaks is also very clear, $D = 3.42 \pm 0.47$. The observed cluster distribution is indeed bimodal!

When we apply the GMM algorithm to our model sample, we also find strong bimodality. In order to keep the sample size similar to the data, we test separately each of the 11 random model realizations of each host halo. The resulting parameters form a set from which we calculate the average parameters. To estimate both the statistical and systematic errors of each parameter, we sum in quadrature its mean standard deviation in the set and the scatter among the realizations. A heteroscedastic split gives $\mu_1 = -1.543 \pm 0.045$, $\sigma_1 = 0.318 \pm 0.043$ and $\mu_2 = -0.576 \pm 0.077$, $\sigma_2 = 0.237 \pm 0.026$. The break-down is 66% ($\pm 4\%$) of the clusters in the metal-poor group and 34% in the metal-rich group. The average separation of the peaks is very significant, $D = 3.44 \pm 0.29$. None of the 1000 parametric bootstrap sets of a unimodal distribution returned any of the three statistics (λ , D , $kurt$) as high as those found the model. Again, a unimodal distribution is rejected at a confidence level better than 0.1%. Thus,

our fiducial metallicity distribution is bimodal as well.

A different methodology to the LRT in the Bayesian approach is the Odds Ratio, or the Bayes factor described in Liddle (2009). The Odds Ratio is the ratio of the integrals of the likelihood function \mathcal{L} over all possible ranges of the model parameters with the corresponding normalized distribution functions of the parameters. In the case of one-Gaussian vs. two-Gaussians, it is $\int \mathcal{L}_2 P(p_1) P(\mu_1) P(\sigma_1) P(\mu_2) P(\sigma_2) dp_1 d\mu_1 d\sigma_1 d\mu_2 d\sigma_2 / \int \mathcal{L}_1 P(\mu) P(\sigma) d\mu d\sigma$. The Odds Ratio is dimensionless and is greater than 1 if the modal split indeed significantly improves the likelihood \mathcal{L}_2 over \mathcal{L}_1 . On the other hand, if the improvement in the likelihood is small, it can be washed out by integration over the additional parameters and the Odds Ratio becomes less than 1. We have experimented with using the Odds Ratio as an objective criterion for the goodness of modal split but found that its application depends sensitively on the adopted range of the parameters and their (unknown) distribution functions. Therefore, we have not included it in our GMM code.

Dip test

A completely independent test of unimodality was proposed by Hartigan & Hartigan (1985). It was first used for globular cluster studies by Gebhardt & Kissler-Patig (1999). The Dip test is based on the cumulative distribution of the input sample. The Dip statistic is the maximum distance between the cumulative input distribution and the best-fitting unimodal distribution. In some sense, this test is similar to KS test but the Dip test searches specifically for a flat step in the cumulative distribution function, which corresponds to a “dip” in the histogram representation. The probability of rejecting a unimodal distribution is calculated empirically and tabulated as a function of sample size. We obtained an updated table of the probabilities calculated recently by Martin Maechler (www.cran.r-project.org/web/packages/diptest).

We have added a driver routine to the original Fortran code of Hartigan & Hartigan (1985). Our code interpolates the probability table for any input sample size up to 5000 objects. Looking just at the significance levels, the Dip test appears less powerful than GMM. The Dip probability of the observed Galactic sample being bimodal is 90%, whereas the LRT probability is 99.998% and the parametric bootstrap probability is 99.9%. However, the Dip test has the benefit of being insensitive to the assumption of Gaussianity and is therefore a true test of modality. It is also much faster to run than the GMM code. We use the Dip probability for assessing bimodality of our model realizations in Section 4.4.

Note that we searched for a statistical method that evaluates bimodality using full input information, without having to bin the data. Another method, RMIX, based on a histogram of the input sample was recently suggested by Wehner et al. (2008).

Source codes of the GMM and Dip tests are available from one of the authors (OG) upon request.

REFERENCES

- Ambartsumian, V. A. 1938, Uch. Zap. Leningrad G. U., 22, 19 [English transl. in IAU Symp. 113, Dynamics of Star Clusters, ed. J. Goodman & P. Hut (Dordrecht: Reidel), 521]
- Ashman, K. M., Bird, C. M., & Zepf, S. E. 1994, AJ, 108, 2348
- Ashman, K. M. & Zepf, S. E. 1992, ApJ, 384, 50
- Bauer, D. J. 2007, Multivariate Behavioral Research, 42, 757
- Baumgardt, H. 2001, MNRAS, 325, 1323
- Baumgardt, H. & Makino, J. 2003, MNRAS, 340, 227
- Beasley, M. A., Baugh, C. M., Forbes, D. A., Sharples, R. M., & Frenk, C. S. 2002, MNRAS, 333, 383
- Bell, E. F., Zheng, X. Z., Papovich, C., Borch, A., Wolf, C., & Meisenheimer, K. 2007, ApJ, 663, 834
- Binney, J. & Tremaine, S. 2008, Galactic Dynamics (Princeton: Princeton University Press)
- Borch, A., Meisenheimer, K., Bell, E. F., Rix, H., Wolf, C., Dye, S., Kleinheinrich, M., Kovacs, Z., & Wisotzki, L. 2006, A&A, 453, 869
- Brodie, J. P. & Strader, J. 2006, ARA&A, 44, 193
- Brooks, A. M., Governato, F., Booth, C. M., Willman, B., Gardner, J. P., Wadsley, J., Stinson, G., & Quinn, T. 2007, ApJ, 655, L17
- Bruzual, G. & Charlot, S. 2003, MNRAS, 344, 1000
- Chernoff, D. F. & Weinberg, M. D. 1990, ApJ, 351, 121
- Conroy, C. & Gunn, J. E. 2010, ApJ, 712, 833
- Conroy, C. & Wechsler, R. H. 2009, ApJ, 696, 620
- Cote, P., Marzke, R. O., & West, M. J. 1998, ApJ, 501, 554
- Crain, R. A., Eke, V. R., Frenk, C. S., Jenkins, A., McCarthy, I. G., Navarro, J. F., & Pearce, F. R. 2007, MNRAS, 377, 41
- Dahlen, T., Mobasher, B., Dickinson, M., Ferguson, H. C., Giavalisco, M., Kretzmer, C., & Ravindranath, S. 2007, ApJ, 654, 172
- Davé, R., Finlator, K., & Oppenheimer, B. D. 2007, EAS Publications Series, Volume 24, 183-189; astro-ph/0608537
- De Angeli, F., Piotto, G., Cassisi, S., Busso, G., Recio-Blanco, A., Salaris, M., Aparicio, A., & Rosenberg, A. 2005, AJ, 130, 116
- Dotter, A., Sarajedini, A., Anderson, J., Aparicio, A., Bedin, L. R., Chaboyer, B., Majewski, S., Marín-Franch, A., Milone, A., Paust, N., Piotto, G., Reid, I. N., Rosenberg, A., & Siegel, M. 2010, ApJ, 708, 698
- Erb, D. K., Shapley, A. E., Pettini, M., Steidel, C. C., Reddy, N. A., & Adelberger, K. L. 2006, ApJ, 644, 813
- Fall, S. M. & Zhang, Q. 2001, ApJ, 561, 751
- Forbes, D. A. & Bridges, T. 2010, MNRAS, 404, 1203
- Forbes, D. A., Brodie, J. P., & Grillmair, C. J. 1997, AJ, 113, 1652
- Fusi Pecci, F., Bellazzini, M., Buzzoni, A., De Simone, E., Federici, L., & Galletti, S. 2005, AJ, 130, 554
- Gebhardt, K. & Kissler-Patig, M. 1999, AJ, 118, 1526
- Georgiev, I. Y., Puzia, T. H., Goudfrooij, P., & Hilker, M. 2010, MNRAS, accepted; arXiv:1004.2039
- Gieles, M. & Baumgardt, H. 2008, MNRAS, 389, L28
- Gnedin, N. Y. 2000, ApJ, 542, 535
- Gnedin, O. Y., Lee, H. M., & Ostriker, J. P. 1999, ApJ, 522, 935
- Griffen, B. F., Drinkwater, M. J., Thomas, P. A., Helly, J. C., & Pimblett, K. A. 2010, MNRAS, accepted; arXiv:0910.0310
- Harris, W. E. 1996, AJ, 112, 1487
- , 2010, Royal Society of London Phil. Trans. Series A, 368, 889
- Harris, W. E. & Pudritz, R. E. 1994, ApJ, 429, 177
- Hartigan, J. A. & Hartigan, P. M. 1985, The Annals of Statistics, 13, 70
- Hénon, M. 1961, Annales d’Astrophysique, 24, 369
- Hoeft, M., Yepes, G., Gottlöber, S., & Springel, V. 2006, MNRAS, 371, 401
- Holtzman, J. A., Faber, S. M., Shaya, E. J., Lauer, T. R., Groth, J., Hunter, D. A., Baum, W. A., Ewald, S. P., Hester, J. J., Light, R. M., Lynds, C. R., O’Neil, E. J., & Westphal, J. A. 1992, AJ, 103, 691
- Hurley, J. R., Pols, O. R., & Tout, C. A. 2000, MNRAS, 315, 543
- Hurley, J. R., Shara, M. M., Richer, H. B., King, I. R., Saul Davis, D., Kalirai, J. S., Hansen, B. M. S., Dotter, A., Anderson, J., Fahlman, G. G., & Rich, R. M. 2008, AJ, 135, 2129
- Kirby, E. N., Simon, J. D., Geha, M., Guhathakurta, P., & Frebel, A. 2008, ApJ, 685, L43
- Kissler-Patig, M., Jordán, A., & Bastian, N. 2006, A&A, 448, 1031
- Komatsu, E., Smith, K. M., Dunkley, J., Bennett, C. L., Gold, B., Hinshaw, G., Jarosik, N., Larson, D., Nolte, M. R., Page, L., Spergel, D. N., Halpern, M., Hill, R. S., Kogut, A., Limon, M., Meyer, S. S., Odegard, N., Tucker, G. S., Weiland, J. L., Wollack, E., & Wright, E. L. 2010, ApJS, submitted, arXiv:1001.4538
- Kravtsov, A. V. & Gnedin, O. Y. 2005, ApJ, 623, 650
- Kravtsov, A. V., Gnedin, O. Y., & Klypin, A. A. 2004, ApJ, 609, 482
- Kravtsov, A. V., Klypin, A. A., & Khokhlov, A. M. 1997, ApJS, 111, 73
- Kroupa, P. 2001, MNRAS, 322, 231
- Kruijssen, J. M. D. 2008, A&A, 486, L21
- Lamers, H. J. G. L. M., Gieles, M., & Portegies Zwart, S. F. 2005, A&A, 429, 173
- Liddle, A. R. 2009, Annual Review of Nuclear and Particle Science, 59, 95
- Lo, Y. 2008, Statistics and Computing, 18, 233
- Lo, Y., Mendell, N. R., & Rubin, D. B. 2001, Biometrika, 88, 767
- Marín-Franch, A., Aparicio, A., Piotto, G., Rosenberg, A., Chaboyer, B., Sarajedini, A., Siegel, M., Anderson, J., Bedin, L. R., Dotter, A., Hempel, M., King, I., Majewski, S., Milone, A. P., Paust, N., & Reid, I. N. 2009, ApJ, 694, 1498
- McGaugh, S. S. 2005, ApJ, 632, 859
- McLachlan, G. J. 1987, Journal of the Royal Statistical Society. Series C (Applied Statistics), 36, 318
- McLaughlin, D. E. 1999, AJ, 117, 2398

- Moore, B., Diemand, J., Madau, P., Zemp, M., & Stadel, J. 2006, *MNRAS*, 368, 563
- Murray, N. & Rahman, M. 2010, *ApJ*, 709, 424
- Muthén, B. 2003, *Psychological Methods*, 8, 369
- Naab, T., Johansson, P. H., & Ostriker, J. P. 2009, *ApJ*, 699, L178
- O'Connell, R. W., Gallagher, J. S., Hunter, D. A., & Colley, W. N. 1995, *ApJ*, 446, L1
- Okamoto, T., Gao, L., & Theuns, T. 2008, *MNRAS*, 390, 920
- Orban, C., Gnedin, O. Y., Weisz, D. R., Skillman, E. D., Dolphin, A. E., & Holtzman, J. A. 2008, *ApJ*, 686, 1030
- Peng, E. W., Jordán, A., Côté, P., Takamiya, M., West, M. J., Blakeslee, J. P., Chen, C.-W., Ferrarese, L., Mei, S., Tonry, J. L., & West, A. A. 2008, *ApJ*, 681, 197
- Press, W. H., Teukolsky, S. A., Vetterling, W. T., & Flannery, B. P. 2007, *Numerical recipes. The art of scientific computing*, 3rd ed. (Cambridge: University Press)
- Prieto, J. L. & Gnedin, O. Y. 2008, *ApJ*, 689, 919
- Puzia, T. H., Perrett, K. M., & Bridges, T. J. 2005, *A&A*, 434, 909
- Rey, S., Rich, R. M., Sohn, S. T., Yoon, S., Chung, C., Yi, S. K., Lee, Y., Rhee, J., Bianchi, L., Madore, B. F., Lee, K., Barlow, T. A., Forster, K., Friedman, P. G., Martin, D. C., Morrissey, P., Neff, S. G., Schiminovich, D., Seibert, M., Small, T., Wyder, T. K., Donas, J., Heckman, T. M., Milliard, B., Szalay, A. S., & Welsh, B. Y. 2007, *ApJS*, 173, 643
- Rhode, K. L., Zepf, S. E., & Santos, M. R. 2005, *ApJ*, 630, L21
- Savaglio, S., Glazebrook, K., Le Borgne, D., Juneau, S., Abraham, R. G., Chen, H., Crampton, D., McCarthy, P. J., Carlberg, R. G., Marzke, R. O., Roth, K., Jørgensen, I., & Murowinski, R. 2005, *ApJ*, 635, 260
- Spitzer, L. R. & Forbes, D. A. 2009, *MNRAS*, 392, L1
- Spitzer, L. 1987, *Dynamical Evolution of Globular Clusters* (Princeton: Princeton University Press)
- Spitzer, L. J. 1940, *MNRAS*, 100, 396
- Spitzer, L. J. & Chevalier, R. A. 1973, *ApJ*, 183, 565
- Stewart, K. R., Bullock, J. S., Wechsler, R. H., & Maller, A. H. 2009, *ApJ*, 702, 307
- Strader, J., Brodie, J. P., Cenarro, A. J., Beasley, M. A., & Forbes, D. A. 2005, *AJ*, 130, 1315
- Strader, J., Smith, G. H., Larsen, S., Brodie, J. P., & Huchra, J. P. 2009, *AJ*, 138, 547
- Tassis, K., Kravtsov, A. V., & Gnedin, N. Y. 2008, *ApJ*, 672, 888
- Tremonti, C. A., Heckman, T. M., Kauffmann, G., Brinchmann, J., Charlot, S., White, S. D. M., Seibert, M., Peng, E. W., Schlegel, D. J., Uomoto, A., Fukugita, M., & Brinkmann, J. 2004, *ApJ*, 613, 898
- Trenti, M., Heggie, D. C., & Hut, P. 2007, *MNRAS*, 374, 344
- Waters, C. Z., Zepf, S. E., Lauer, T. R., & Baltz, E. A. 2009, *ApJ*, 693, 463
- Wehner, E. M. H., Harris, W. E., Whitmore, B. C., Rothberg, B., & Woodley, K. A. 2008, *ApJ*, 681, 1233
- Whitmore, B. C., Zhang, Q., Leitherer, C., Fall, S. M., Schweizer, F., & Miller, B. W. 1999, *AJ*, 118, 1551
- Wolfe, J. H. 1971, in *Technical Bulletin STB 72-2* (San Diego: U.S. Naval Personnel and Training Research Laboratory)
- Woo, J., Courteau, S., & Dekel, A. 2008, *MNRAS*, 390, 1453
- Zepf, S. E. & Ashman, K. M. 1993, *MNRAS*, 264, 611
- Zepf, S. E., Ashman, K. M., English, J., Freeman, K. C., & Sharples, R. M. 1999, *AJ*, 118, 752
- Zinn, R. 1985, *ApJ*, 293, 424